


Article

Surface Modifications of Superparamagnetic Iron Oxide Nanoparticles with Polyvinyl Alcohol, Chitosan, and Activated Carbon or Graphite as Methylene Blue Adsorbents—Comparative Study

Linh Doan ^{1,2,3,*} , Tu M. D. Nguyen ^{1,2,3}, Tan M. Le ^{1,2,3}, Khanh G. Huynh ^{1,2,3} and Tran P. T. Quach ^{1,2,3}

¹ Department of Chemical Engineering, International University—Vietnam National University, Ho Chi Minh City 70000, Vietnam

² Nanomaterials Engineering Research & Development (NERD) Laboratory, International University—Vietnam National University, Ho Chi Minh City 70000, Vietnam

³ School of Chemical and Environmental Engineering, International University—Vietnam National University, Ho Chi Minh City 70000, Vietnam

* Correspondence: dhlinh@hcmiu.edu.vn

Abstract: Adsorption is a popular technique and has been investigated with many different materials for removing synthetic dyes from textile wastewater. This study compares the methylene blue (MB) adsorption capabilities of surface-modified superparamagnetic iron oxide nanoparticles, (SPION) using polyvinyl alcohol (PVA) and chitosan (CS), combined with two carbon materials, activated carbon (AC) and graphite (GR), respectively. After 9 days, depending on the initial MB loading concentration (0.015 mg/mL, 0.02 mg/mL, and 0.025 mg/mL), the MB adsorption capacities onto SPION/PVA/CS/AC and SPION/PVA/CS/GR were 7.6 ± 0.2 – 22.4 ± 0.05 and 6.9 ± 0.02 – 22.4 ± 0.05 mg/g, respectively. The cumulative release percentages of SPION/PVA/CS/AC and SPION/PVA/CS/GR after 30 days were $63.24 \pm 8.77\%$ – $22.10 \pm 2.59\%$ and $91.29 \pm 12.35\%$ – $24.42 \pm 1.40\%$, respectively. Additionally, both SPION/PVA/CS/AC and SPION/PVA/CS/GR can both fit the Freundlich isotherm model. The adsorption and desorption kinetics can be fitted to the pseudo-second-order linear and zeroth-order models, respectively. At 0.020 mg/mL MB initial loading, out of SPION/PVA/CS/AC, SPION/PVA/CS/GR, and SPION/PVA/CS/GO, SPION/PVA/CS/AC is the most economical adsorbent. Compared to SPION/PVA/AC, SPION/PVA/CS/AC is less economical. Since CS has antimicrobial properties, antimicrobial activities should be investigated to conclude which adsorbent is more promising: SPION/PVA/AC or SPION/PVA/CS/AC.

Keywords: adsorption; iron oxide nanoparticles; nanocomposites; isotherm; kinetics; carbon



Citation: Doan, L.; Nguyen, T.M.D.; Le, T.M.; Huynh, K.G.; Quach, T.P.T. Surface Modifications of Superparamagnetic Iron Oxide Nanoparticles with Polyvinyl Alcohol, Chitosan, and Activated Carbon or Graphite as Methylene Blue Adsorbents—Comparative Study. *Coatings* **2023**, *13*, 1797. <https://doi.org/10.3390/coatings13101797>

Received: 28 September 2023

Revised: 14 October 2023

Accepted: 18 October 2023

Published: 20 October 2023



Copyright: © 2023 by the authors. Licensee MDPI, Basel, Switzerland. This article is an open access article distributed under the terms and conditions of the Creative Commons Attribution (CC BY) license (<https://creativecommons.org/licenses/by/4.0/>).

1. Introduction

Water contamination is a significant issue on a worldwide scale. Among them, eutrophication of waterbodies and falling-off in water quality are two environmental challenges associated with wastewater discharge. Synthetic dyes, which are produced globally in quantities of 7×10^7 tons annually, are one of the leading causes of water pollution globally each year due to their non-biodegradable properties [1]. An average of 20% of the synthetic textile dyes used each year are lost during production and processing, and these dyes end up in the environment as a result of effluents from the treatment of leftover industrial water [2]. These textile dyes have various types, such as acid, basic, azo, direct, disperse, reactive, sulfur, and vat [2]. Textile dyes, especially methylene blue (MB), greatly reduce the prerequisite for biochemical and chemical oxygen, the impairment of photosynthesis, the suppression of plant development, access to the food chain, recalcitrance and bioaccumulation, and their vulnerability to poisoning, mutagenicity, and malignancy [3,4]. One of

the ways to prevent the amount of dye molecules lost to effluents is a synthetic dye made to ensure that they are all bonded to the fiber [5].

There are several approaches to treating dye effluents, including adsorption, ion exchange, flocculation, decantation, advanced oxidation processes, biodegradation, chemical precipitation, and other processes [6]. Among all of these techniques, adsorption has gained popularity for being an attractive option since, depending on the system, it is efficient, cost-effective, and simple to handle materials [7]. Sorption comes in two different varieties. Physical sorption, which is reversible in nature and has low enthalpy values, is the term used to describe the sorption phenomena when weak van der Waals forces dominate. In contrast, when a sorbate and sorbent molecule form chemical bonds, this sorption process is called chemisorption [2]. One study shows that the mechanism of adsorption on the adsorbent during removal involves the following four steps: (1) Progressive transport: moving solute from bulk solution to immobilized membrane by forward or axial dispersion or diffusion. (2) Membrane transfer: osmosis and cohesion of solute particles in a fixed aqueous film. (3) Mass transfer: the binding of solute particles to the surface of the adsorbent extra. And finally, (4) intraparticle diffusion: movement of the solute into the adsorbent and intraparticle diffusion holes [8,9].

Out of all of these MB treatments, adsorption is the most common technique. To absorb MB, nanotechnology was recently implemented. To ease the recovery of the adsorption process, magnetic properties were used to modify the adsorbents [10]. To obtain magnetic properties, superparamagnetic iron oxide nanoparticles (SPION) can be utilized. In short, superparamagnetism is the phenomenon that nanoparticle magnetism may randomly reverse direction under the effect of temperature if their size is small enough and the measurement time for the nanoparticles' magnetization is substantially longer than the Neel relaxation time when no external field is present [11]. These nanocarriers are successfully removed from the human body through the iron metabolism pathway and are non-toxic, biodegradable, and biocompatible [12]. Out of all iron oxide nanoparticles (IONPs), including magnetic (SPION or Fe_3O_4), maghemite ($\gamma\text{-Fe}_2\text{O}_3$), and hematite ($\alpha\text{-Fe}_2\text{O}_3$), only SPION exhibits superparamagnetism at the nanoscale [12–15]. Superparamagnetic NPs can be applied to various fields by modifying the surface with various materials [11]. To avoid aggregation and stabilize the NPs, SPION can be coated with a layer of organic compounds (i.e., acids, polysaccharides, or polymers) [16]. Nevertheless, several investigations have demonstrated that some undesired SPION aggregates may have lower stability, biocompatibility, and effectiveness. As a result, the use of SPION in conjunction with other stabilizing tools, such as carbon compounds, has been researched [6,10,17–31].

Specifically, to enhance the adsorption capacities, SPION is usually modified with carbon-based materials. To remove MB from wastewater, SPION has various material combinations. Without any modifications, SPION has an adsorption capacity of 45.43 mg/mL at pH = 12 and T = 298 K [20]. By changing to pH = 7 and adding polymer and GO, the adsorption of SPION/PVA/CS/GO decreased slightly, to approximately 37 mg/mL [6]. In addition, there were some positive results with some of the products, such as the combination product SPION@Carbon sheets, which increased to 95 mg/g at very high temperatures, such as 400 °C, or SPION/EG modeled by Redlich–Peterson and PSO, which exhibited an adsorption value of 75 mg/mL compared to pure SPION [21–24]. SPION@C using bergamia orange gave good results, with an adsorption of 141.3 mg/g [32]. SPION/GO had the highest ratio with 280.26 mg/g [25]. Since then, a number of material combinations with SPION to improve and enhance some features as well as save costs have also been implemented. From there, they are compared in all aspects and can be easily applied in many fields.

As MB adsorbents in wastewater treatment, carbon-based materials should be inexpensive and abundant. Additionally, the synthesis process should be facile. Hence, out of all of these carbon-based materials, two candidates stand out the most in terms of low cost, high adsorption capacities, and easy synthesis: activated carbon (AC) and graphite (GR).

In a variety of chemical and physical processes, the adsorption capacity of activated carbon has been discovered to prevail over that of other materials for the removal of dyes from aqueous solutions in terms of methodology, the ability to effectively adsorb a variety of different types of adsorbates, and the cost-effective adsorbent design [33]. In situations where particular hydraulic considerations must be made, they are advised for the general removal of organic molecules from water. In order to use activated carbons in their most common applications, sorbents with a lot of extremely small holes are needed [34]. The quantity of adsorbed material on the macropore surface is small compared to that for the micropores, which means that the existence of micropores significantly impacts their sorption characteristics [35]. Therefore, in adsorption technologies, one of the most critical steps is to characterize the activated carbons [35]. Due to its enormous surface area, high level of surface reactivity, and widespread availability of material, activated carbon has received a lot of support as a very effective adsorbent in wastewater treatment [36]. Both organic and inorganic chemicals that are pollutant adsorption are subject to their utilization. Activated carbon may be made from a variety of agricultural byproducts and wastes, including bamboo, wood, coconut shells, and rice husks [36].

On the other hand, graphite has a large surface area and is also a low-cost and plentiful material, making it an appealing alternative for water treatment applications [37–41]. Graphite is also the most stable carbon, which consists of graphene layers [42,43]. Within each layer, the layer can produce weak van der Waals interactions because the delocalized pi-orbital links the metallic and covalent bonding [42,43]. Hence, by inserting atoms or molecules between the graphene layers, the adsorption process can be improved drastically [42,43]. Hence, modifying SPION with graphite is necessary to improve the adsorption process of synthetic dyes from the textile wastewater industry, especially methylene blue, which can cause mutation, cancer, and dermal disease [44–46].

In addition to carbon-based materials, polymers can be introduced into the adsorbents. The benefits of introducing polymers include a potential reduction in agglomeration and several other surface-related issues. Additionally, a good polymer mix can considerably enhance SPION's characteristics [47–49]. Hence, out of all of these polymers, chitosan (CS) and polyvinyl alcohol (PVA) were used in the composite.

Extracted from cretaceous shells, chitosan is a non-toxic and biodegradable polymer [50,51]. Additionally, many researchers have found antimicrobial activities of CS against *Helicobacter pylori*, *Staphylococcus aureus*, and *Escherichia coli* [52,53]. Hence, CS is regarded as a material that is ecologically benign and biocompatible, helps to lower production costs, and works well as an adsorbent for the treatment of waste and water. As a highly selective natural adsorbent with several functional groups, including amine ($-\text{NH}_2$) and hydroxyl ($-\text{OH}$) groups, it possesses sufficient active sites to collect contaminants and strong chelating properties. Because the polymer matrix contains amine groups, it can interact with contaminating ions in a solution through ion exchange or other complexation events [51]. At low pH, chitosan can adsorb heavy metals (i.e., Cu^{2+} , Cd^{2+} , Pb^{2+} , and Cr^{6+}) and dyes [54]. Chitosan also forms gels under acidic conditions ($\text{pH} < 5.5$), making the hydroxyl and amine groups inaccessible to the metal bond [54]. In order to enhance chemical stability in acidic environments, components should be added. Research was conducted on the use of chitosan and Fe_3O_4 to remediate the chromium in wastewater. The chromium removal effectiveness of the chitosan–magnetite nanocomposite reached 92.33% in the presence of magnetite nanoparticles, as opposed to roughly 29.4% for CS alone. The obvious outcome of combining CS with SPION may have promise for wastewater treatment, as one may infer [55]. In addition, chitosan has been demonstrated to possess antibacterial properties against a number of bacterial species. Chitosan's antibacterial action is influenced by a number of variables, such as the molecular weight, level of deacetylation, concentration, and the particular bacterial species that it is most effective against. Higher molecular weight and deacetylation levels in chitosan have been proven in studies to have stronger antibacterial activity. Additionally, chitosan's antibacterial action can be improved by boosting the concentration. Chitosan's positively charged glucosamine

groups interact with the negatively charged bacterial or fungal cell membranes to cause internal components to flow out, which is how it exerts its antibacterial effect [52,56–58]. Although chitosan has been demonstrated to have antibacterial action, it is important to note that it may or may not be useful in eliminating particular compounds from wastewater, such as methylene blue. Chitosan's capacity to remove methylene blue or kill bacteria in wastewater is influenced by a number of variables, including the chitosan content, contact duration, pH, and the unique properties of the wastewater [59].

On the other hand, polyvinyl alcohol (PVA) is a hydrophilic, inexpensive, water-soluble, non-toxic, and biodegradable polymer [60,61]. As a linear polymer, polyvinyl alcohol (PVA) can be cross-linked using various methods, such as irradiation, thermal cycling, and chemical agents like glutaraldehyde, which can increase its mechanical strength and stability in aqueous environments [62–65]. PVA can be strengthened by CS by means of adding more active sites through the hydrogen bonds it forms with the amine groups. The high water adsorption, which is viewed as a drawback when employing PVA as a membrane or composite, is, however, caused by the presence of the hydroxyl group in the structure. Several researchers have sought to use adjuvants to optimize membrane usage in order to decrease the solubility of PVA [66]. PVA is added to the chitosan structure to enhance the chemical stability in the acidic environment of the compound. In addition, PVA and CS work well together to create a polymer that has enhanced mechanical qualities, antibacterial activity, and moisture retention, making it a potential material for wound healing applications [67]. PVA/CS blended films have been demonstrated to successfully remove MB and inhibit bacteria in wastewater in the context of wastewater treatment. In comparison to pure CS, it was discovered that mixing PVA with CS in any amount greatly increased the swelling of the resulting films. Additionally, CS can gain additional desired features when combined with PVA, such as enhanced mechanical properties, biocompatibility, and biodegradability. This is mostly due to the ease with which a wide range of synthetic and natural polymers may be combined, the abundance of possibilities available, and the fact that it is effective in practical applications [68,69].

The novelty of this work is to determine the inexpensive, easy-to-recover, efficient, and easy-to-synthesize adsorption capabilities of SPION-based adsorbents. In this work, the simplicity of the synthesis method can be seen via the reaction conditions (i.e., room temperature and pressure) and abundant materials (i.e., ferrous salt, ferric salt, activated carbon, and graphite). The synthesis was simply mixing, stirring, and drying. Hence, the current work evaluates the potential for MB adsorption and desorption onto SPION-based composites employing polymer blends and carbon-based materials. Therefore, the SPION/PVA/CS/AC and SPION/PVA/CS/GR were synthesized, and the MB adsorption/desorption capabilities were investigated and compared to the SPION/PVA/CS/GO, SPION/PVA/GR, and SPION/PVA/AC, which were previously published [6,17,31].

2. Materials and Methods

2.1. Materials

All the materials were purchased within the same batch and from sources similar to previous publications [6,31]. Additionally, activated carbon (AC) was purchased from Shanghai Zhanyun Chemical Co., Ltd. (Shanghai, China). As received, all chemicals were used without any further purification.

The synthesis of superparamagnetic iron oxide nanoparticles (SPION): similar to published research, using a co-precipitation method without any modifications, SPION was synthesized [6,48,70,71].

The synthesis of SPION/PVA/CS/AC and SPION/PVA/CS/GR: First, PVA/CS were synthesized similarly to the literature [6]. Then, SPION and AC or SPION and GR were introduced with the same mass, same mass ratio, and same techniques as in the literature [6].

2.2. Characterization

Similar to previous publications, the successful creation of the SPION/PVA/CS/AC and SPION/PVA/CS/GR materials was characterized using Fourier transform infrared spectroscopy (FTIR, Bruker Sensor 27, Ettlingen, Germany), field emission scanning electron microscopy (FE-SEM, Hitachi SU8000, Tokyo, Japan), a vibrating sample magnetometer (VSM), the Barrett–Joyner–Halenda (BJH) method, and X-ray diffraction (XRD) [6,31].

2.3. Determining the Adsorption and Desorption Capacity of Methylene Blue on SPION/PVA/CS/AC and SPION/PVA/CS/GR

Similar to previous publications, the adsorption and desorption capacities of MB onto the adsorbents (SPION/PVA/CS/AC and SPION/PVA/CS/GR) were carried out three times [6].

2.4. Determining the Adsorption Kinetics, Adsorption Isotherm, and Desorption Kinetics

From the adsorption experiments, adsorption capacities (Q_t), loading capacity (%LC), entrapment efficiency (%EE), adsorption kinetics (pseudo-first order linear/non-linear, pseudo-second order linear/non-linear, simplified Elovich), intraparticle diffusion, and adsorption isotherms (Langmuir and Freundlich) were calculated. The desorption experiments can be used to illustrate the desorption kinetics (Korsmeyer–Peppas, Higuchi, and zeroth order). These mentioned parameters and various others can be calculated using equations that were published previously [6,31,72].

3. Results and Discussion

3.1. Characterization of SPION/PVA/CS/AC and SPION/PVA/CS/GR

3.1.1. FE-SEM Analysis

FE-SEM (Hitachi SU8000, Tokyo, Japan) was used to characterize the IONPs, as shown in Figure 1.

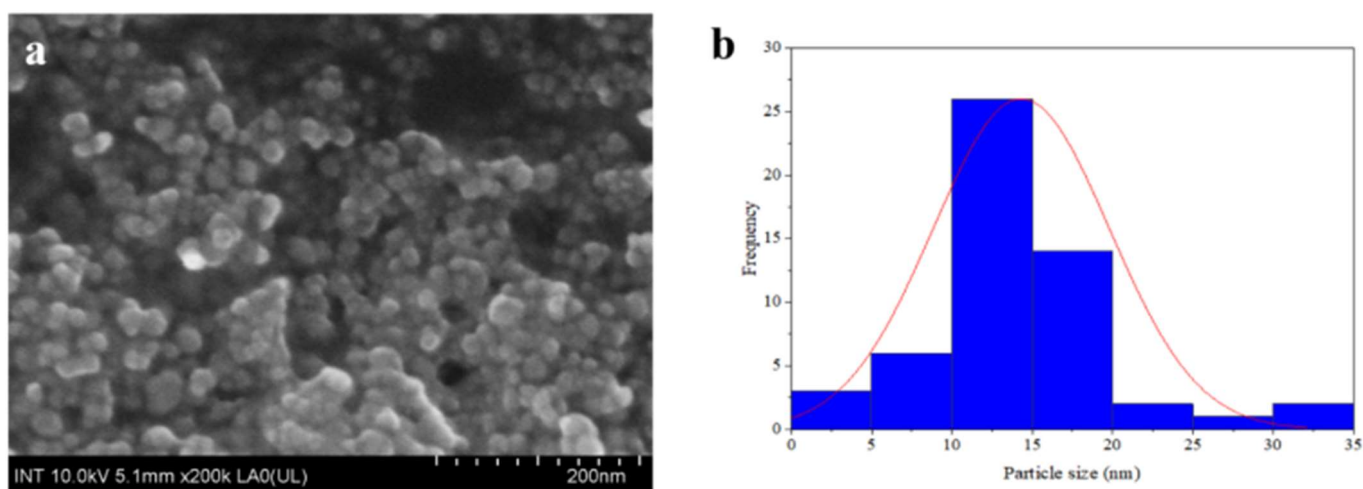


Figure 1. (a) FE-SEM image of IONPs in 200 nm. (b) The normal size distribution of IONPs.

As shown in Figure 1, the morphology of the synthesized adsorbents can be observed. The agglomeration was evident, similarly to a prior study. As shown in Figure 1b, similar to previous publications, the average size of IONPs was 14.4 ± 4.8 nm [6,48,70,71]. After the synthesis of IONPs, PVA/CS and AC or GR were introduced, and the adsorbents were also characterized using FE-SEM, as shown in Figure 2.

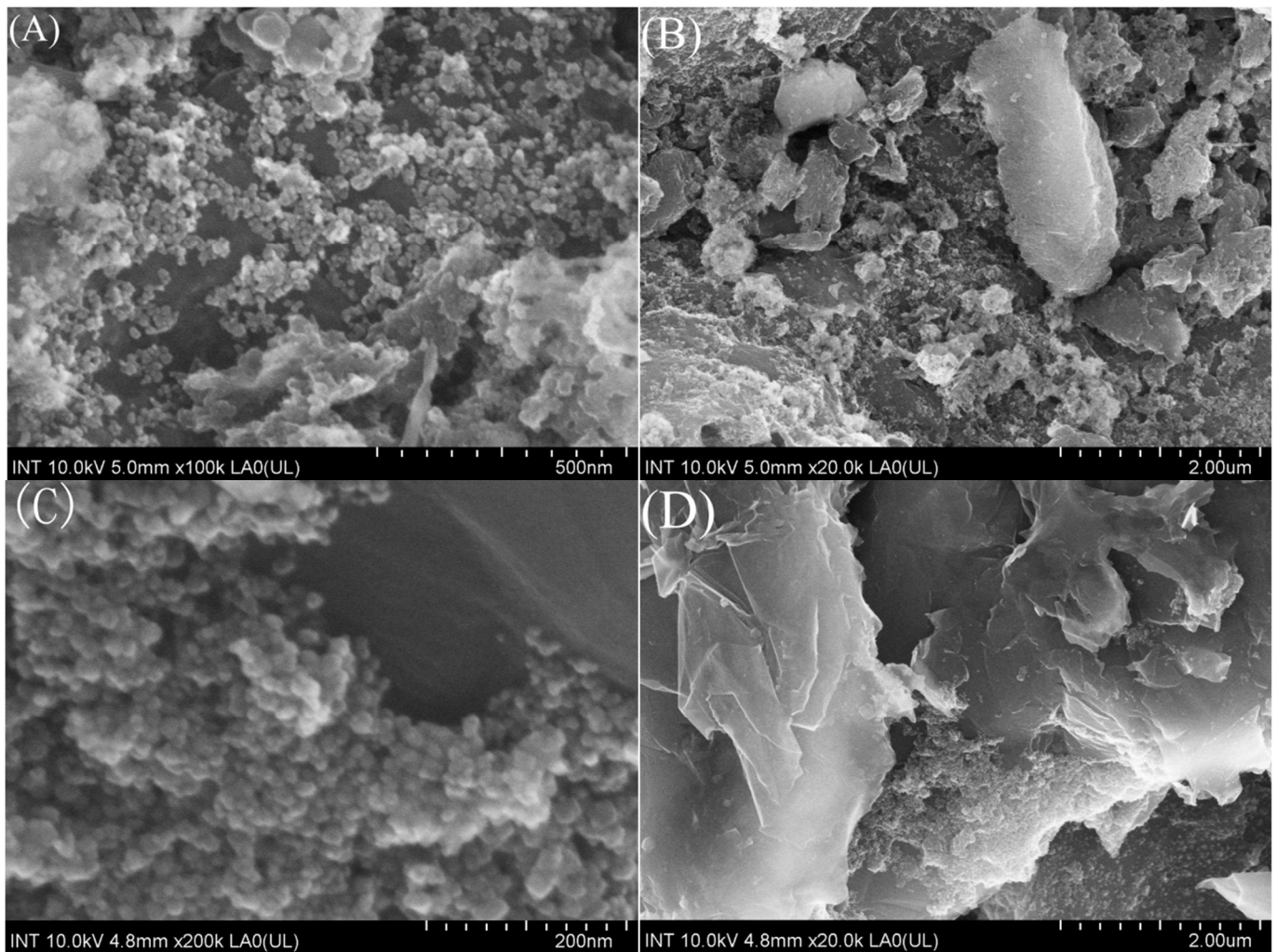


Figure 2. FE-SEM images of SPION/PVA/CS/AC (A) 500 nm and (B) 1 μm ; SPION/PVA/CS/GR (C) 500 nm and (D) 1 μm .

Figure 2A,C indicate that SPION has been aggregated, but there is no appearance of polymer. The possibility could be SPION-coated PVA/CS, so further confirmation by XRD and FTIR is needed. However, the sheets found could be either AC or GR, as it is difficult to distinguish by observation alone, so they need to be characterized by FTIR and XRD.

3.1.2. XRD Analysis

To determine the classification of IONPs in the samples, XRD was used to determine the crystal structure as well as the crystallite size of the materials. According to the results shown in Figure 3, the peaks appeared at 2θ positions of 30.22° , 35.58° , 43.22° , 53.68° , 57.27° , and 62.85° , which are denoted as being correlated with the magnetite (based on the corresponding hkl indices), similar to previous publications [6,17,31]. It can be concluded that the IONPs presented in the materials were SPION, and the mixture of materials with SPION can be proved to be a successful blend according to the similar peaks shown in the diffractograms.

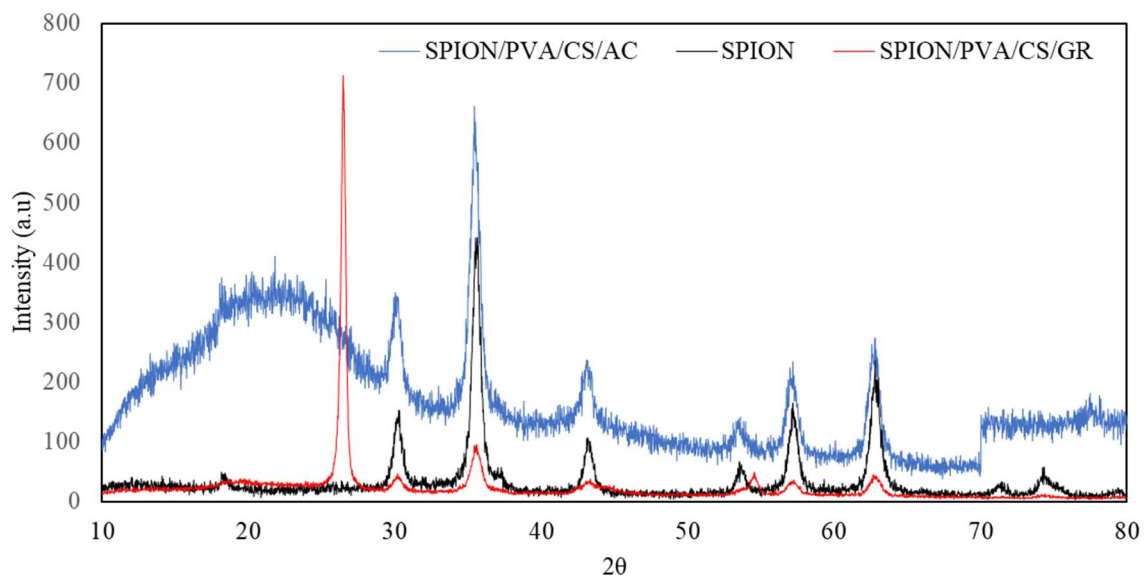


Figure 3. Overlay XRD diffractograms of SPION, SPION/PVA/CS/AC, and SPION/PVA/CS/GR.

3.1.3. FTIR Analysis

The functional groups presented in nanoparticles and the structure of the adsorbents were determined by FTIR using the same method as in previous publications [6,17,31]. The two samples of SPION/PVA/CS/AC and SPION/PVA/CS/GR were analyzed by FTIR analysis, and the results are shown in Figure 4 and Table 1.

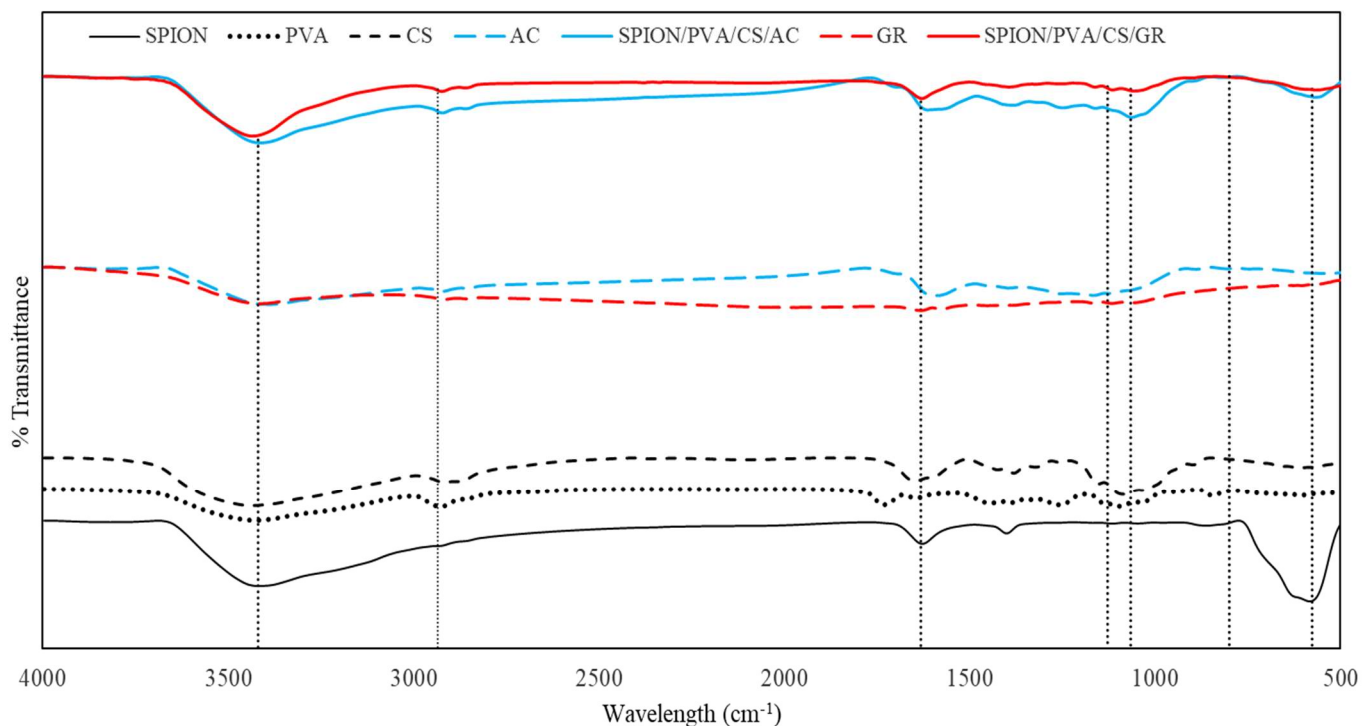


Figure 4. FTIR spectra of SPION, PVA, CS, AC, GR, SPION/PVA/CS/AC, and SPION/PVA/CS/GR.

As shown in Figure 4 and Table 1, the peaks of SPION, PVA, CS, AC, and GR were obtained by FTIR analysis. The intensity of O–H stretching vibration was noticeably high due to the low concentration of the diluted sample in water. However, distinguishing characteristics can be noticed among the components. For example, the vibration Fe–O of SPION, C–H wagging and O–H bending modes of PVA, C–N stretching and C–H bond

in the pyranose ring of CS, C=C stretching in the aromatic ring of AC, and C–O stretching of the alkoxy group of GR.

Table 1. FTIR analysis of SPION, PVA, CS, AC, GR, SPION/PVA/CS/AC, and SPION/PVA/CS/GR.

Materials	Peaks (cm ⁻¹)	Functional Group	Ref.
SPION	3419	O–H symmetric stretching	[73,74]
	1629	Carbonyl C=O stretching band	[73,74]
	587	Vibration Fe–O	[73–75]
	447	Vibration Fe–O	[75,76]
PVA	3397	O–H symmetric stretching	[77,78]
	2944	CH ₂ asymmetric stretching	[78–80]
	1736	C=O stretching band	[79–81]
	1657	O–H bending mode of OH groups	[80,82,83]
	1440	CH ₂ bending	[78–80,82]
	1330	CH wagging	[80]
	1266	C–O–C stretching	[84]
	1145	C–O stretching	[78,80,82,85]
	1098	C–O stretching	[78,80,82,85]
	947	CH ₂ rocking	[80]
	853	C–C stretching	[80,82]
CS	3425	O–H symmetric stretching and –NH symmetrical vibration	[78,86]
	2923	C–H symmetric stretching	[86–88]
	1650	C=O stretching of amide I	[86–89]
	1423	C–H bending	[88]
	1382	CH ₂ in CH ₂ OH group	[90]
	1323	C–N stretching of amide III	[86]
	1262	C–H bond in the pyranose ring	[90]
	1157	C–O–C asymmetric stretching Saccharide structure of chitosan	[86,88,91]
	1077	C–O stretching	[78,88,92]
	1030	C–O stretching	[86,88]
897	Saccharide structure of chitosan	[78,91]	
AC	3390	O–H stretching vibration	[93,94]
	2920	C–H stretching vibration	[94]
	2855	C–H stretching vibration	[94]
	1593	C=C stretching vibration in aromatic rings	[95]
	1396	C–H stretching vibration C–O–H bending vibration	[93]
	1166	C–O–H stretching vibration	[95]
	807	C–C stretching vibration	[95]

Table 1. Cont.

Materials	Peaks (cm^{-1})	Functional Group	Ref.	
GR	3422	O–H stretching vibration	[96–98]	
	2919	CH_2 asymmetric stretching	[96]	
	2856	CH_2 symmetric stretching	[96]	
	1632	C=C stretching vibration	[96,98]	
	1165	C–O stretching vibration	[99]	
	1116	C–O stretching vibration	[99]	
	1065	C–O stretching of alkoxy group	[96,98]	
SPION/ PVA/CS/ AC	3414	O–H stretching vibration	This research	
	2923	CH_2 asymmetric vibration C–H symmetric stretching	This research	
	1614	C=O stretching band O–H bending mode of OH groups	This research	
	1384	C–H stretching vibration C–O–H bending vibration CH_2 in CH_2OH group	This research	
	1248	C–O–C stretching C–H bond in the pyranose ring	This research	
	1160	C–O stretching C–O–C asymmetric stretching Saccharide structure of chitosan C–O–H stretching vibration	This research	
	1064	C–O stretching	This research	
	569	Vibration Fe–O	This research	
	SPION/ PVA/CS/ GR	3434	O–H stretching vibration	This research
		2924	CH_2 asymmetric vibration C–H symmetric stretching	This research
2860		CH_2 symmetric stretching	This research	
1629		C=O stretching band C=C stretching vibration	This research	
1395		CH_2 in CH_2OH group CH wagging	This research	
1162		C–O–C asymmetric stretching Saccharide structure of chitosan C–O stretching vibration	This research	
1115		C–O stretching vibration	This research	
1058		C–O stretching of alkoxy group C–O stretching	This research	
565		Vibration Fe–O	This research	

Figure 4 and Table 1 show that the spectra of SPION displayed peaks at approximately 3419 and 1629 cm^{-1} , which are related to the O–H symmetric stretching and C=O stretching bands of the carbonyl group accordingly. It is believed that there was Fe–O vibration at 587 and 447 cm^{-1} .

The given spectra of PVA gave the band of adsorption as follows: O–H symmetric stretching at 3397 cm^{-1} , CH_2 asymmetric stretching at 2944 cm^{-1} , C=O stretching and O–H bending modes at 1736 and 1657 cm^{-1} , respectively, CH_2 bending at 1440 cm^{-1} , C–H wagging at 1330 cm^{-1} , and C–O–C stretching at 1266 cm^{-1} . Moreover, C–O stretching

vibration was also found at 1145 and 1098 cm^{-1} , while CH_2 rocking and C–C stretching can be seen at 947 cm^{-1} and 853 cm^{-1} , respectively.

According to the FTIR spectrum of CS, it can be observed that there was a noticeable peak at 3425 cm^{-1} , which corresponds to O–H symmetric stretching and –NH symmetric vibration. It appears that the other peaks were assigned to C–H symmetric stretching at 2923 cm^{-1} , C=O stretching of amide I at 1650 cm^{-1} , C–H bending at 1423 cm^{-1} , CH_2 in the CH_2OH group at 1382 cm^{-1} , and C–N stretching of amide III and the C–H bond in the pyranose ring at 1323 and 1262 cm^{-1} , respectively. The peak at 1157 cm^{-1} is expected to be the C–O–C asymmetric stretching and saccharide structure of chitosan, both at 1157 and 897 cm^{-1} . C–O stretching is also found at 1077 and 1030 cm^{-1} .

The band of adsorption that is related to AC and gives the vibrations at different wavelengths can be identified, such as O–H symmetric stretching at 3390 cm^{-1} , C–H stretching at 2920 and 2855 cm^{-1} , C=C stretching of aromatic rings at 1593 cm^{-1} , C–H stretching and C–O–H bending at 1396 cm^{-1} , C–O–H stretching at 1166 cm^{-1} , and C–C stretching at 807 cm^{-1} .

The vibrational spectrum of GR gives the appearance of distinguished peaks. Firstly, the O–H stretching band can be observed at 3422 cm^{-1} , while CH_2 asymmetric and symmetric stretching were assigned at 2919 and 2856 cm^{-1} , respectively. C=C stretching vibration is seen at peak 1632 cm^{-1} . C–O stretching vibration can be observed at both 1165 and 1116 cm^{-1} vibrational peaks. Lastly, the C–O stretching of the alkoxy group is found at a wavelength of 1065 cm^{-1} .

The FTIR spectra of both samples, SPION/PVA/CS/AC and SPION/PVA/CS/GR, are summarized in Figure 4 and Table 1, with the presence of peaks that are denoted to be the same as the components. To be more specific, with SPION/PVA/CS/AC, the O–H stretching vibration can be found at 3414 cm^{-1} , which is the same group in SPION, PVA, CS, and AC. The noticeable peak at 2923 cm^{-1} is assigned to CH_2 asymmetric and symmetric vibrations as PVA, CS, and AC. The peak at 1614 cm^{-1} showed the C=O stretching band of SPION or the O–H bending mode of PVA. At 1384 cm^{-1} , C–H stretching and C–O–H bending were the same as AC, while CH_2 stretching of the CH_2OH group is believed to be similar to CS. C–O–C stretching and C–H in the pyranose of CS can be found at the peak of 1248 cm^{-1} . Next, the peak at 1160 cm^{-1} gives the characteristic C–O stretching of PVA, C–O–C asymmetrical vibration of CS, and C–O–H stretching of AC. The distinguished characteristic of SPION is also found at the peak of 569 cm^{-1} , which is presented as the vibration of Fe–O.

Similarly, with the sample of SPION/PVA/CS/GR, the outstanding peak of O–H stretching was found at 3434 cm^{-1} , which can also be found in other components. CH_2 asymmetric and C–H symmetric stretching are found at 2924 cm^{-1} , as were the peaks in the spectra of PVA, CS, and GR. CH_2 symmetry is presented by the peak at 2860 cm^{-1} , as in the GR spectrum. The peak at 1629 cm^{-1} shows the appearance of the C=O stretching band (CS) and C=C stretching vibration (GR), while CH_2 of the CH_2OH group in CS and C–H wagging in PVA can also be observed at 1395 cm^{-1} . C–O–C asymmetric stretching of the CS structure and C–O stretching of GR can be noticed at 1162 cm^{-1} . Furthermore, the vibration of Fe–O, which is remarkable in SPION, can be found at the peak of 565 cm^{-1} in the spectrum.

To sum up, the FTIR analysis gives proof that both of the samples were successfully blended and synthesized with each of the components.

3.1.4. VSM Analysis

The magnetic characteristics of SPION, SPION/PVA/CS/AC, and SPION/PVA/CS/GR were carried out by VSM analysis at room temperature, which can be obtained by the S-shaped curves among the magnetic field without coercivity of remanence. As a result, in Figure 5, VSM analysis proves that the IONPs were superparamagnetic [100].

The maximum saturation magnetization (M_s) for the three samples, SPION, SPION/PVA/CS/GR, and SPION/PVA/CS/AC, were found to be 66.29 M_s , 12.96 M_s , and

7.25 M_s , respectively. The decrease in magnetization could be explained by the layers of polymers covering the SPION that lead to the shell coating of polymers [101].

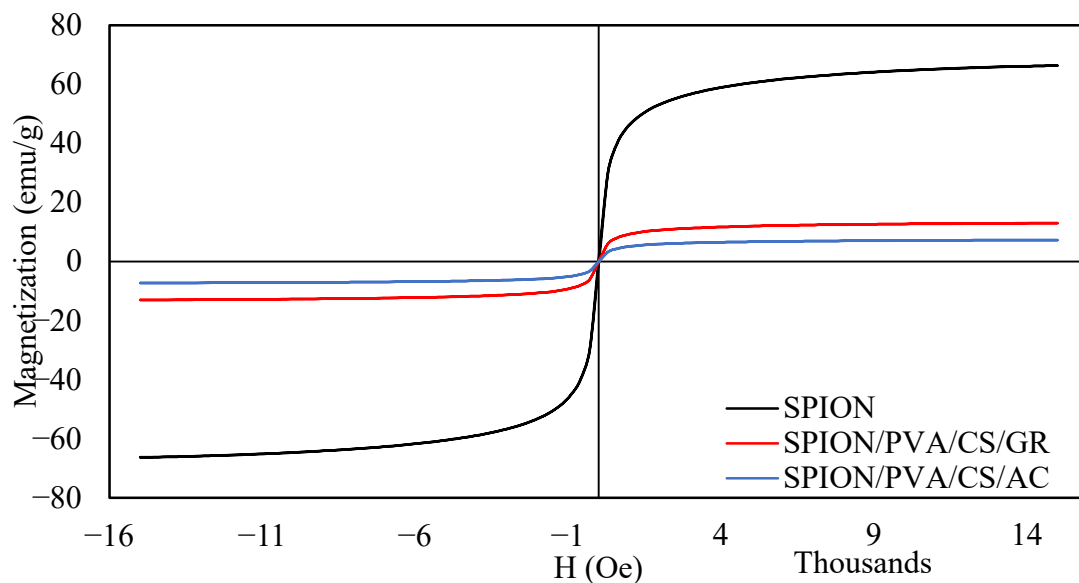


Figure 5. Magnetization properties of SPION, SPION/PVA/CS/AC, and SPION/PVA/CS/GR using VSM.

According to the previous studies [102,103], SPION's result matched the figure of the superparamagnetism graph and the range of M_s given in Figure 5. This could conclude that the SPION in this study was successfully synthesized. Moreover, it could be seen that adding polymers could lower the magnetization of the magnetic material; however, it was still in the paramagnetic range.

3.1.5. BJH Analysis

As shown in Figure 6, the adsorption-desorption isotherm illustrates the increase in the volume of adsorbate uptake of the two materials.

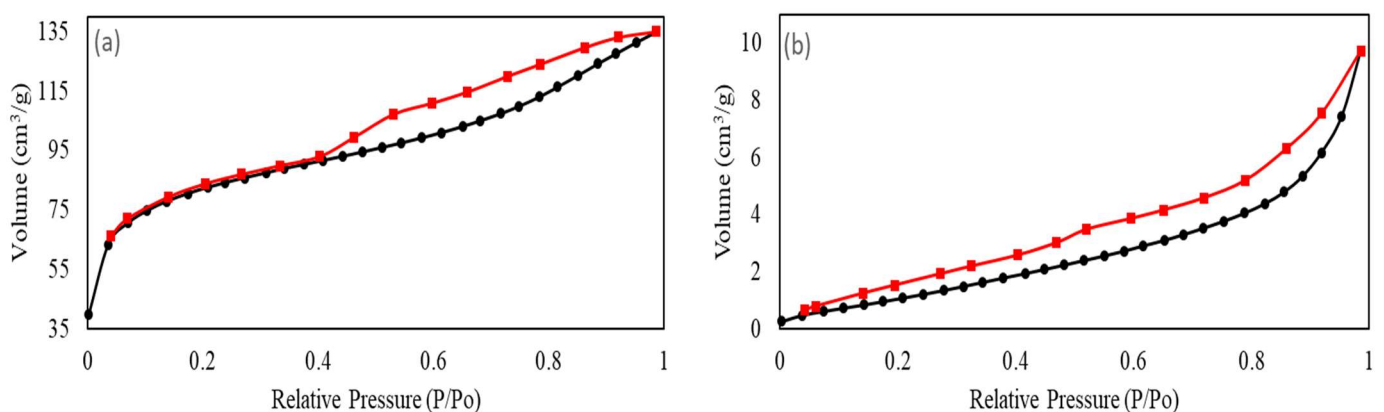


Figure 6. BJH result of (a) SPION/PVA/CS/AC and (b) SPION/PVA/CS/GR.

According to Figure 6, for SPION/PVA/CS/GR, the BJH result yields the type III isotherm, indicating the materials have a low adsorption capacity [104]. On the other hand, the mesoporous structure of SPION/PVA/CS/AC was indicated as type IV isotherm, which indicates that the material has a pore size between 2 nm and 50 nm [104]. In addition, the type IV isotherm shows that the maximum amount of adsorption occurs before saturation

pressure and a hysteresis loop is related to the existence of intermediate porosity [104,105]. The pore diameter and volume of the two materials are summarized in Table 2 as follows:

Table 2. BJH and BET analysis of SPION/PVA/CS/AC and SPION/PVA/CS/GR.

	SPION/PVA/CS/AC	SPION/PVA/CS/GR
Surface area (m ² /g)	563.891	8.059
Pore diameter (Å)	9.719	27.516
Pore volume (cm ³ /g)	0.251	0.017

As shown in Table 2, the surface areas of SPION/PVA/CS/AC and SPION/PVA/CS/GR are measured to be 563.891 and 8.059 m²/g, respectively, using BJH and BET analysis. Comparing these surface areas, SPION/PVA/CS/AC has a surface area 69.97% greater than SPION/PVA/CS/GR. Another factor is that the pore volume of SPION/PVA/CS/AC is 0.251 cm³/g, while SPION/PVA/CS/GR's pore has a volume of 0.017 cm³/g. This shows that SPION/PVA/CS/AC is 14.76% greater than SPION/PVA/CS/GR. Lastly, the mean diameter of both materials is also measured to be 9.719 Å of SPION/PVA/CS/AC and 27.516 Å of SPION/PVA/CS/GR. This indicates that SPION/PVA/CS/GR is 2.83% smaller than SPION/PVA/CS/AC.

3.2. Adsorption

Similar to previous publications, using UV-VIS spectroscopy, Q_t , %LC, and %EE were evaluated, as shown in Table 3 [6,17,31].

Table 3. The Q_t , %LC, and %EE of SPION/PVA/CS/AC and SPION/PVA/CS/GR adsorbing methylene blue after 310 h.

Material	Initial MB Concentration (mg/mL)	Q_t (mg/g)	%LC (%)	%EE (%)
SPION/PVA/CS/AC	0.015	7.6 ± 0.2	0.76 ± 0.02	30.3 ± 0.7
	0.02	14.9 ± 0.1	1.5 ± 0.01	44.8 ± 0.4
	0.025	22.4 ± 0.05	2.2 ± 0.005	53.7 ± 0.1
SPION/PVA/CS/GR	0.015	6.9 ± 0.02	0.69 ± 0.002	27.7 ± 0.09
	0.02	14.5 ± 0.01	1.45 ± 0.001	43.4 ± 0.03
	0.025	22.2 ± 0.004	2.22 ± 0.0004	53.3 ± 0.009

As shown in Table 3 and Figure 7a, the adsorption capacity of SPION/PVA/CS/AC after 310 h was 7.6 ± 0.2 mg/g, 14.9 ± 0.1 mg/g, and 22.4 ± 0.05 mg/g at MB concentrations of 0.015 mg/mL, 0.02 mg/mL, and 0.025 mg/mL, respectively.

Additionally, as shown in Figure 7c, the entrapment efficiency of the MB that was adsorbed with SPION/PVA/CS/AC was 30.28%, 44.82%, and 53.70% in different concentrations of MB 0.015, 0.02, and 0.025 mg/mL, respectively, after 310 h at room temperature.

Compared to SPION/PVA/CS/GR, as shown in Figure 8, the MB trapping efficiency at three different concentrations (0.015 mg/mL, 0.02 mg/mL, and 0.025 mg/mL) was 27.66%, 43.36%, and 53.30%, respectively. After 310 h of adsorption, it can be seen that the two carbon materials' trapping efficiencies were similar (about 2.62% at a concentration of 0.015 mg/mL), and the difference between the two concentrations was quite noticeable (about 15%), while the difference between 0.02 and 0.025 was about 9%.

According to the obtained result, it can be concluded that the concentration has a noticeable effect of on adsorption capacity. It is shown that the higher initial MB concentration along with more abundant free adsorption sites are approachable, which leads to a dramatic increase in adsorption capacity until reaching equilibrium state [106].

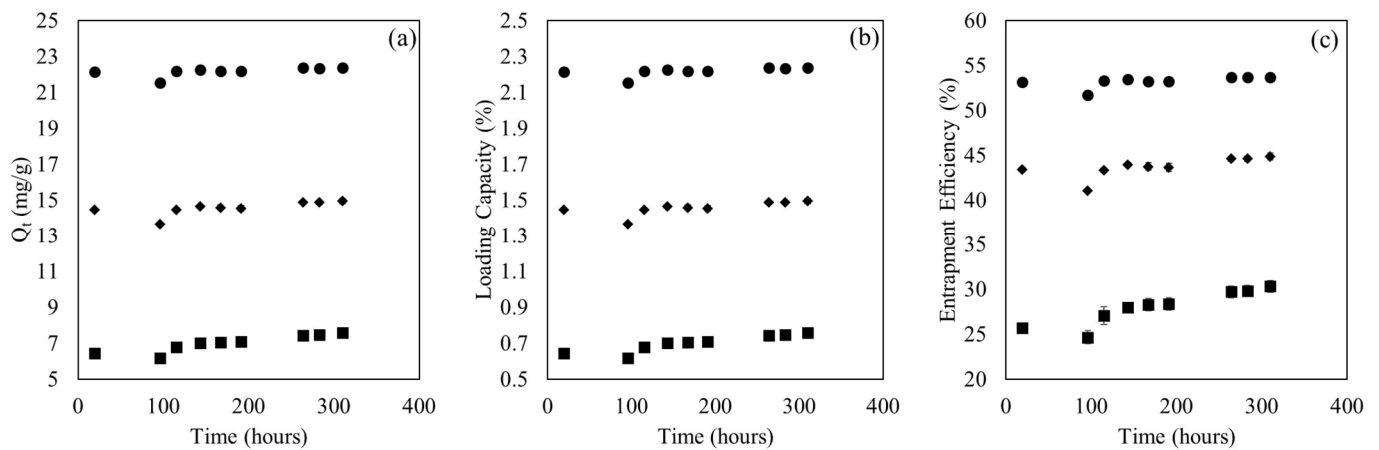


Figure 7. (a) Adsorption amount over time, (b) loading capacity over time, and (c) entrapment efficiency over time of SPION/PVA/CS/AC. Square: initial conc. MB 0.015 mg/mL, diamond: initial conc. MB 0.020 mg/mL, circle: initial conc. MB 0.025 mg/mL.

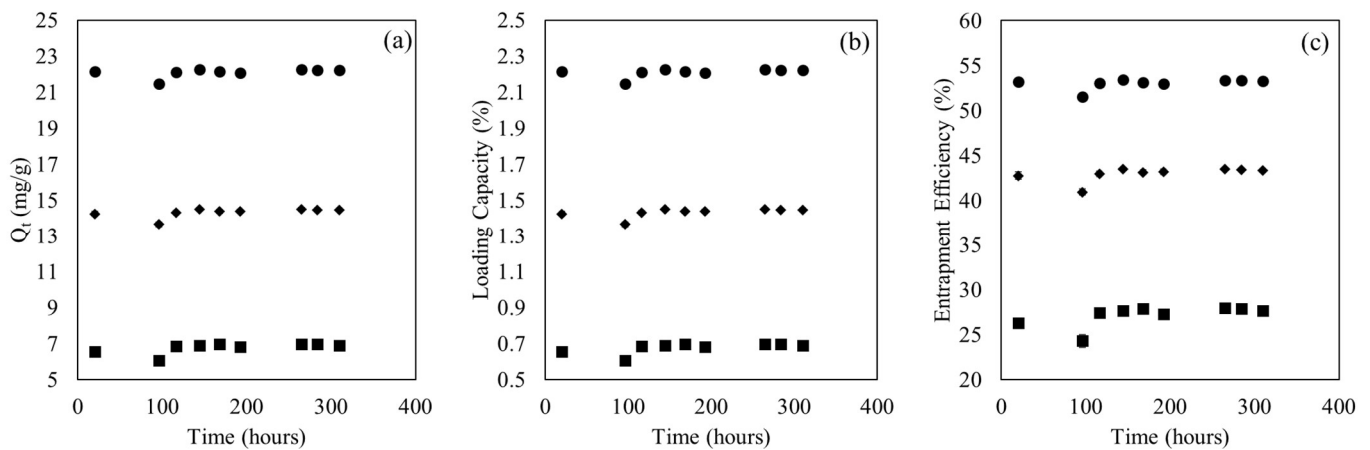


Figure 8. (a) Adsorption amount over time, (b) loading capacity over time, and (c) entrapment efficiency over time of SPION/PVA/CS/GR. Square: initial conc. MB 0.015 mg/mL, diamond: initial conc. MB 0.020 mg/mL, circle: initial conc. MB 0.025 mg/mL.

From Table 3 and Figure 7, the highest adsorption capacities occurred at a MB concentration of 0.025 mg/mL. At this concentration, SPION/PVA/CS/AC and SPION/PVA/CS/GR were similar to each other (53.7 ± 0.1 mg/g and 53.3 ± 0.009 mg/g, respectively). As shown in Figure 8, after 143 h of adsorption, it can be observed that the adsorption amount of MB was nearly reaching equilibrium at 6.991, 14.654, and 22.266 mg/g in three concentrations, respectively. After 310 h, the loading capacities of the three concentrations were accordingly 7.6, 14.9, and 22.4 mg/g, which can be considered to be slowly increasing with the longer time span.

As shown in Figure 8, the growth of %EE is very slight among the three concentrations. To be more specific, the %EE for concentrations of 0.02 and 0.025 mg/mL increased by approximately 0.01% from 115 h to 191 h and from 264 h to 310 h, while with 0.015 mg/mL, the %EE was unchanged from 115 to 191 h; however, there was a hardly noticeable increase in the %EE of the next time span, which was calculated to be only 0.02%.

According to Figure 8, it is clear that with SPION/PVA/CS/GR, the concentration affected the loading capacity of MB, which at first increased slightly, then reached equilibrium until, 310 h later, desorption occurred, which led to a decrease in loading capacity and entrapment efficiency.

After 96 h of adsorption, the increase in loading capacity of all three concentrations was about 0.8%, while with the longer experimental time, this growth was more stable

among these concentrations. The highest loading capacities were obtained after 284 h, which were calculated as 0.697%, 1.448%, and 2.223% at the concentrations of 0.015, 0.02, and 0.025 mg/mL, respectively. Subsequently, it appears that there was a decrease in the loading capacity with a time of 310 h. It can be explained that after reaching the equilibrium state from 116 to 284 h, the materials start to cause desorption, releasing MB.

The same pattern can be observed with entrapment efficiency, which is provided in Figure 8, with the maximum of %EE obtained after 265 h. Specifically, the %EE of each concentration was 27.949%, 43.543%, and 53.393%, respectively. The further experimental time span led to a drop in %EE after the adsorption had reached equilibrium.

By using pseudo-first-order, pseudo-second-order, and simplified Elovich kinetic models with different initial concentrations of MB, the rate of adsorption as well as the loading amount at equilibrium were calculated as shown below.

From Tables 4 and 5, the linear pseudo-second order can be considered to be the best-fit model of both SPION/PVA/CS/AC and SPION/PVA/CS/GR for adsorbing MB at three initial concentrations of 0.015, 0.020, and 0.025 mg/mL. This is due to the high R^2 values compared to the high χ^2 in pseudo-first order non-linear and pseudo-second order non-linear and low R^2 values of simplified Elovich, as shown in Figure 9.

Table 4. Kinetic models of SPION/PVA/CS/AC adsorbing methylene blue after 310 h.

		Initial MB Concentration (mg/mL)		
		0.015	0.020	0.025
Pseudo-first order non-linear	Q_e mg MB (g particles) ⁻¹	13.3	22.3	29.01
	k_1 (g mg ⁻¹ day ⁻¹)	1	1	1
	χ^2	27.2	24.1	14.5
Pseudo-second order non-linear	Q_e mg MB (g particles) ⁻¹	13.3	22.3	29.01
	k_2 (g mg ⁻¹ day ⁻¹)	171.8	56.2	915.9
	χ^2	27.2	24.1	14.5
Pseudo-second order linear	Q_e mg MB (g particles) ⁻¹	22.5	15.1	7.8
	k_2 (g mg ⁻¹ day ⁻¹)	0.6	0.3	0.2
	R^2	0.999	0.999	0.996
Simplified Elovich	α (mg/(g day))	2425.46	116,289.7	419,458.8
	β (mg/g)	2.277	1.354	0.950
	R^2	0.452	0.325	0.292

In accordance with pseudo-second-order kinetic models for both materials, the adsorption process can be concluded to be chemisorption, in which MB adsorbed onto the surface of the materials due to the valence forces between MB and each material [107,108]. Moreover, the values of k_i and I were calculated, as shown in Table 6, showing that the intraparticle diffusion process can be used to regulate the adsorption capacity of MB onto SPION/PVA/CS/AC and SPION/PVA/CS/GR.

Table 5. Kinetic models of SPION/PVA/CS/GR adsorbing methylene blue after 310 h.

		Initial MB Concentration (mg/mL)		
		0.015	0.020	0.025
Pseudo-first order non-linear	Q_e mg MB (g particles) ⁻¹	13.3	22.3	29.01
	k_1 (g mg ⁻¹ day ⁻¹)	1	1	1
	χ^2	28.9	25.5	14.8
Pseudo-second order non-linear	Q_e mg MB (g particles) ⁻¹	13.3	22.3	29.01
	k_2 (g mg ⁻¹ day ⁻¹)	171.8	56.2	915.9
	χ^2	28.9	25.5	14.8
Pseudo-second order linear	Q_e mg MB (g particles) ⁻¹	22.3	14.6	7.1
	k_2 (g mg ⁻¹ day ⁻¹)	0.8	0.7	0.6
	R ²	0.999	0.999	0.998
Simplified Elovich	α (mg/(g day))	140,135.3	512,001.3	1,076,154.2
	β (mg/g)	3.100	1.506	0.9914
	R ²	0.235	0.303	0.287

Table 6. The intraparticle diffusion model of SPION/PVA/CS/AC and SPION/PVA/CS/GR adsorbing methylene blue.

Materials	Initial MB Concentration (mg/mL)	k _I	I	R ²
SPION/PVA/CS/AC	0.015	0.5	5.7	0.782
	0.020	0.3	13.8	0.382
	0.025	0.2	21.8	0.253
SPION/PVA/CS/GR	0.015	0.2	6.2	0.358
	0.020	0.2	13.9	0.256
	0.025	0.1	21.8	0.117

As illustrated in Table 6, the intraparticle diffusion pattern demonstrates that $I \neq 0$, which indicates that this adsorption involves higher intraparticle diffusion. Similar to SPON/PVA/CS/GO, SPION/PVA/CS/AC and SPION/PVA/CS/GR also adsorb MB by means of hydrogen bonding between negatively and positively charged surfaces during electrostatic interactions and via π - π^* stacking with the aromatic ring of MB [6,109,110].

After determining the adsorption kinetics, Langmuir and Freundlich isotherm models were also evaluated, as shown in Table 7.

As shown in Table 7, for the Langmuir model, with R² values higher than 0.94, this model can be considered to fit the adsorption experimental data of SPION/PVA/CS/AC and SPION/PVA/CS/GR. This indicates that between adjacent adsorbed molecules, the lateral interaction does not exist when a single surface site is occupied by a single molecule [72]. However, since the value of R_L > 1, the adsorption can be considered unfavorable. However, the negative K_L value, which is the constant, has no physical meaning and is unaccept-

able [17,111]. Therefore, the Langmuir model should not be considered to fit the experimental data. In contrast to the Langmuir model, with an $R^2 > 0.99$, the Freundlich model could be considered to be fitted to the adsorption experimental data of both adsorbents. For the Freundlich model, which describes heterogeneous and multi-layer adsorption [72,112,113], with $n_F < 1$, the adsorption process can be considered favorable, with the bond energies increasing with surface density [72,112,113]. Additionally, because $1/n_F > 1$, the adsorption process can be considered to be cooperative adsorption, a non-favorable physical process, and a poor adsorption characteristic [72,112,114].

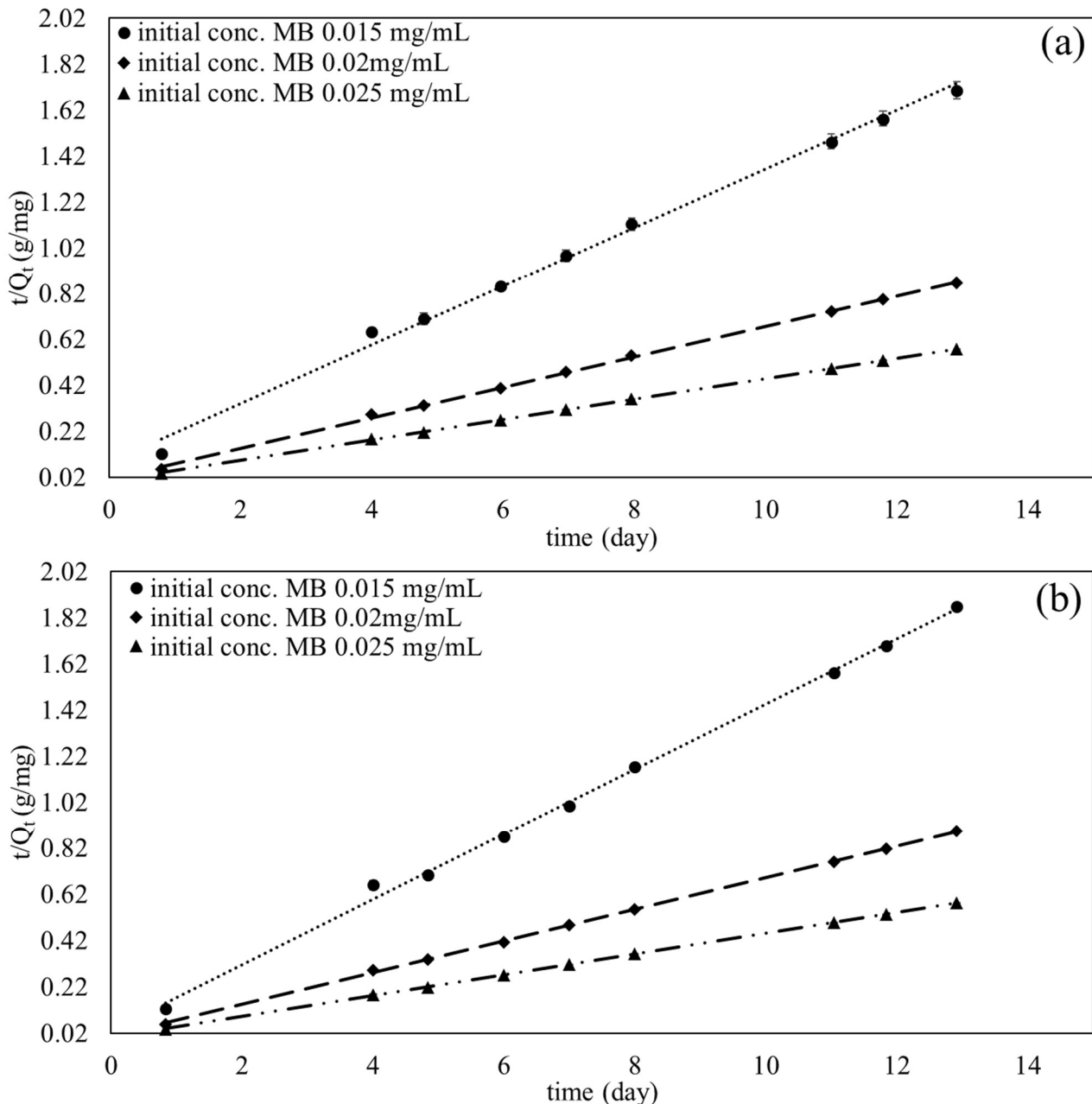


Figure 9. Pseudo-second-order model of (a) SPION/PVA/CS/AC and (b) SPION/PVA/CS/GR adsorbing methylene blue.

Table 7. Adsorption isotherm models' constant and variables.

Model	Constant	SPION/PVA/CS/AC	SPION/PVA/CS/GR
Langmuir	k_L (L/mg)	−12.06	−11.98
	Q^0 (mg/g)	1.06	0.68
	Average R_L	1.32 ± 0.09	1.32 ± 0.09
	R^2	0.94	0.96
Freundlich	k_F (mg/g)	9.55×10^{-11}	1.69×10^{-6}
	$\frac{1}{n_F}$ (mg/L)	10.71	16.05
	R^2	0.99	0.99

3.3. Desorption

The coefficient of release based on initial loading with constant temperature, MB concentration, and a pH of 3.8 is shown in Table 8.

Table 8. The percentage of release average of MB from SPION/PVA/CS/AC and SPION/PVA/CS/GR after 30 days.

Materials	Concentration (mg/mL)	% Release Average
SPION/PVA/CS/AC	0.015	63.24 ± 8.77
	0.02	27.17 ± 3.53
	0.025	22.10 ± 2.59
SPION/PVA/CS/GR	0.015	91.29 ± 12.35
	0.02	39.51 ± 4.37
	0.025	24.42 ± 1.40

Based on Table 8, it can be determined that the highest release rate at 0.015 mg/mL of loaded MB in both carbon materials is 63.24% and 91.29%, respectively. This shows that for the two carbon materials, as the MB concentration increases, the cumulative release percentage decreases. This indicates that SPION/PVA/CS/GR has a cumulative release percentage of 140% higher than SPION/PVA/CS/AC at a MB concentration of 0.015 mg/mL. However, at an initial MB loading concentration of 0.025 mg/mL, the cumulative release percentage of SPION/PVA/CS/AC is less than 2.32%, compared to SPION/PVA/CS/GR. Then, Figure 10 and Table 9 were determined based on mechanism examination and desorption kinetic analysis, combined with cumulative release percentage, desorption kinetic model, and chi-square value.

Table 9. The Korsmeyer–Peppas, 0th order, and Higuchi calculation for the desorption of SPION/PVA/CS/AC and SPION/PVA/CS/GR for methylene blue.

	Korsmeyer–Peppas (KP)		0th Order	Higuchi	KP	χ^2	
	k	n	k	K		0th order	Higuchi
SPION/PVA/CS/AC							
0.015	3.6	0.8	0.004	0.02	68.80	0.020	0.102
0.02	1.4	0.8	0.004	0.02	28.88	0.013	0.114
0.025	1.2	0.8	0.004	0.02	23.69	0.024	0.104
SPION/PVA/CS/GR							
0.015	6.9	0.7	0.006	0.03	101.03	0.027	0.095
0.02	1.9	0.8	0.005	0.02	43.62	0.018	0.140
0.025	1.4	0.8	0.005	0.02	26.51	0.020	0.111

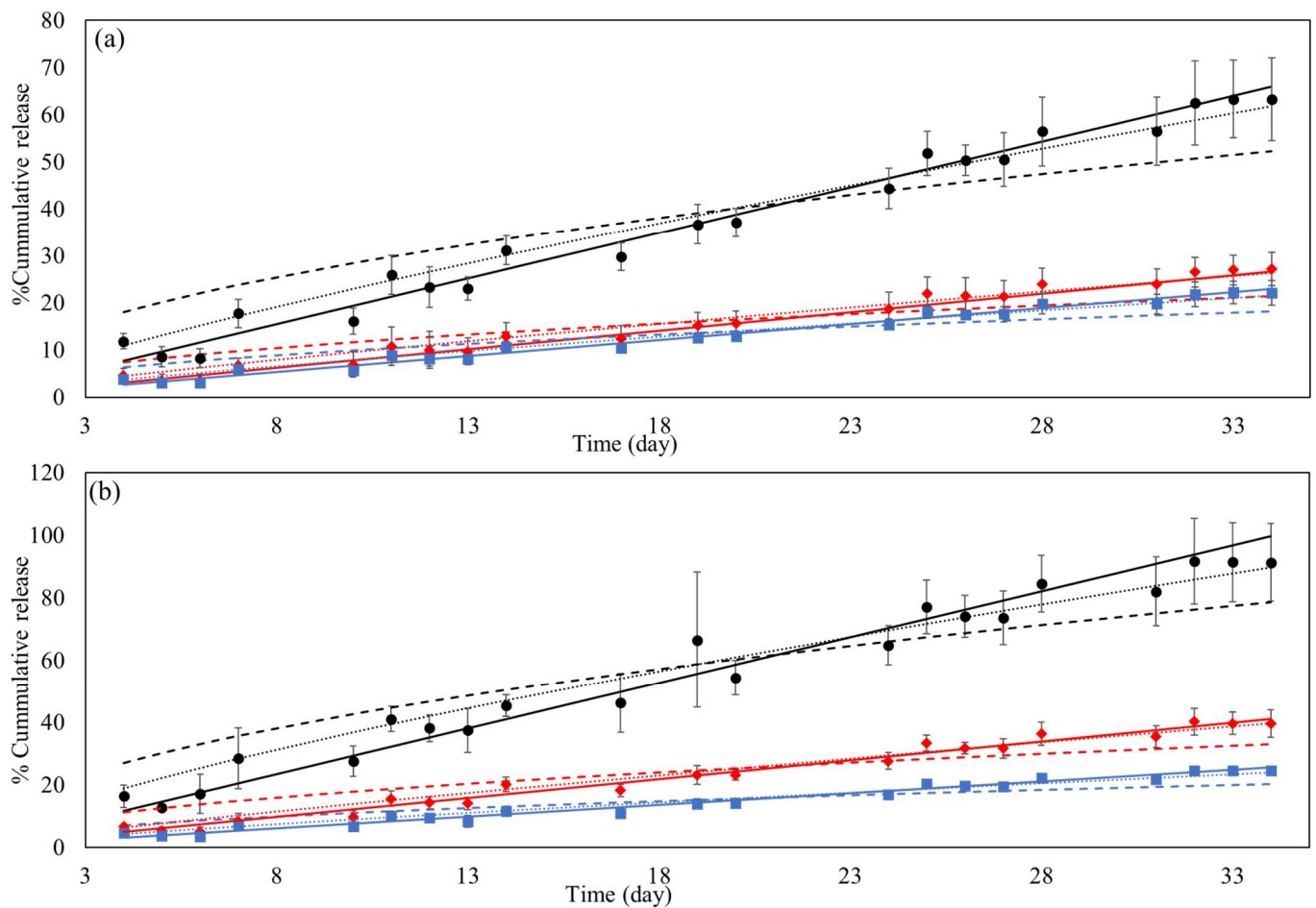


Figure 10. The releasing kinetics after 30 days of MB on (a)—SPION/PVA/CS/AC and (b)—SPION/PVA/CS/GR. Dotted line: KP. Dashed line: Higuchi. Solid line: Zeroth order. Black: initial conc. MB 0.015 mg/mL. Red: initial conc. MB 0.020 mg/mL. Blue: initial conc. MB 0.025 mg/mL.

According to Table 9, with the lowest χ^2 values, the zeroth-order kinetics model can be considered to be the best-fitted desorption model for SPION/PVA/CS/AC and SPION/PVA/CS/GR. The rate is unaffected by changes in the concentration of the reactants. This indicates that diffusion through the pores and fissures of the adsorbents regulates the diffusion process. Anomaly diffusion, or non-Fickian diffusion, which combines diffusion with case-II relaxation, is another option for the releasing process [6,31].

3.4. Comparison

According to the BJH results, SPION/PVA/CS/GO had a surface area of 5.8 m²/g, a pore diameter of 10 Å, and a pore volume of 0.017 cm³/g [6]. In general, the surface area of SPION/PVA/CS/AC is much larger than that of SPION/PVA/CS/GR and SPION/PVA/CS/GO (approximately 98%), while the pore diameters of SPION/PVA/CS/AC and SPION/PVA/CS/GO have similarities and are not too different from SPION/PVA/CS/GR. In particular, SPION/PVA/CS/GO and SPION/PVA/CS/GR have the same pore volume and are about 14.76% smaller than SPION/PVA/CS/AC.

As shown in the previous publication, the adsorption capacities of SPION/PVA/CS/GO stood at 36.39 mg/g at a concentration of 0.025 mg/mL [6]. This indicates that the adsorption capacities of SPION/PVA/CS/AC and SPION/PVA/CS/GR were smaller than those of SPION/PVA/CS/GO by 33.62% and 34.02%, respectively.

In contrast to the adsorption of SPION/PVA/CS/GO, both SPION/PVA/CS/AC and SPION/PVA/CS/GR had superior cumulative release rates at all three different MB con-

centrations. Different from AC and GR, the cumulative release rate of SPION/PVA/CS/GO peaked at 8.94 ± 0.66 , at a concentration of 0.02 mg/mL, but this result was still poor with SPION/PVA/CS/AC (about 3.04%) and SPION/PVA/CS/GR (about 4.42%) at the same concentration [6]. Hence, when taking the ratio of cost to cumulative release percentage, SPION/PVA/CS/AC is still the most promising MB adsorbent at an initial MB loading concentration of 0.025 mg/mL. Release kinetic models from the two materials in Table 9 were used to confirm and ascertain this.

The price of the material, whether expensive or cheap, also contributes to the decision of the material used to treat dyeing wastewater most effectively and at the least cost. In this study, the costs of five materials are compared in Table 10: SPION/PVA/AC, SPION/PVA/GR, SPION/PVA/CS/AC, SPION/PVA/CS/GR, and SPION/PVA/CS/GO. The synthesis methods of SPION/PVA/AC, SPION/PVA/GR, and SPION/PVA/CS/GO have been presented in previous research articles [6,17,31].

Table 10. Economics analysis between SPION/PVA/AC, SPION/PVA/GR, SPION/PVA/CS/AC, SPION/PVA/CS/GR, and SPION/PVA/CS/GO adsorbing MB at initial MB concentration of 0.02 mg/mL and 298.15 K.

Adsorbents	Costs (VND/g)	Adsorption Capacity (mg/g)	%EE (%)	%LC (%)	Adsorption Capacity/Costs (g/VND)
SPION/PVA/AC	681.89	21.75	57.22	2.53	31.90
SPION/PVA/GR	1376.63	19.87	42.30	1.99	14.43
SPION/PVA/CS/AC	1211.5	14.9	44.80	1.50	12.30
SPION/PVA/CS/GR	1761.5	14.5	43.40	1.45	8.23
SPION/PVA/CS/GO	22,551.5	28.768	86.30	2.88	1.28

As shown in Table 10, since SPION/PVA/AC, SPION/PVA/GR, SPION/PVA/CS/AC, SPION/PVA/CS/GR, and SPION/PVA/CS/GO were researched by the same author and the chemicals were purchased from the same batch and companies, the costs of each adsorbent were calculated [6,17,31].

From Table 10, the economics analysis was evaluated to compare the MB adsorption capacity of SPION/PVA/AC, SPION/PVA/GR, SPION/PVA/CS/AC, SPION/PVA/CS/GR, and SPION/PVA/CS/GO when adsorbing an initial MB concentration of 0.02 mg/mL at 298.15 K.

Among SPION/PVA/CS/AC, SPION/PVA/CS/GR, and SPION/PVA/CS/GO, all three adsorbents were synthesized using the same techniques, same chemical batch, and same chemical mass. Taking the ratio of adsorption amount (mg/g) and the cost of AC, GR, and GO, SPION/PVA/CS/AC has the lowest ratio, indicating that SPION/PVA/CS/AC is the most promising MB adsorbent when adsorbing MB at 0.020 mg/mL. However, when the adsorbent consists of CS, the ratio of adsorption capacity and costs is reduced by 159.35% and 17.36% compared to SPION/PVA/CS/AC, SPION/PVA/AC, and SPION/PVA/GR, respectively. However, when comparing the desorption capacities, SPION/PVA/CS/AC can desorb 34.17% more than SPION/PVA/GR. Therefore, between SPION/PVA/CS/AC and SPION/PVA/GR, SPION/PVA/CS/AC can be considered to be a more well-rounded adsorbent. When compared to SPION/PVA/CS/AC, SPION/PVA/AC has higher adsorption capacities, entrapment efficiency, loading capacity, and the ratio of adsorption capacity to costs. This indicates that SPION/PVA/AC can be considered to be the most efficient adsorbent. However, CS also has antimicrobial properties. Hence, antimicrobial activity research should be investigated to conclude which adsorbent is better: SPION/PVA/AC or SPION/PVA/CS/AC.

4. Conclusions

Activated carbon (AC) and graphite (GR), in combination with superparamagnetic iron oxide nanoparticles (SPION) coated with polyvinyl alcohol (PVA) and chitosan (CS) polymers, may be employed as methylene blue (MB) adsorbents. The size of the synthetic SPIONs was 14.4 ± 4.8 nm. Depending on the initial MB concentration of 0.015, 0.020, and 0.025 mg/mL on SPION/PVA/CS/AC, after 9 days, the entrapment efficiency, loading capacity, and loading amounts had a range of $30.3 \pm 0.7\%$ – $53.7 \pm 0.1\%$, $0.76 \pm 0.02\%$ – $2.2 \pm 0.005\%$, and 7.6 ± 0.2 – 22.4 ± 0.05 mg/g, respectively. Similarly, with SPION/PVA/CS/GR, the entrapment efficiency, loading capacity, and loading amounts had a range of $27.7 \pm 0.09\%$ – $53.3 \pm 0.009\%$, $0.69 \pm 0.002\%$ – $2.22 \pm 0.0004\%$, and 6.9 ± 0.02 – 22.2 ± 0.004 mg/g, respectively.

At a pH of 3.8, after 30 days, the cumulative release percentages of AC and GR had a range of $22.10 \pm 2.59\%$ – $63.24 \pm 8.77\%$ and $24.42 \pm 1.40\%$ – $91.29 \pm 12.35\%$, respectively. At 0.020 mg/mL MB initial loading, out of SPION/PVA/CS/AC, SPION/PVA/CS/GR, and SPION/PVA/CS/Graphene Oxide, SPION/PVA/CS/AC is the most economical adsorbent. Compared to SPION/PVA/AC, SPION/PVA/CS/AC is less economical. Since CS has antimicrobial properties, antimicrobial activity research should be investigated to conclude which adsorbent is more promising: SPION/PVA/AC or SPION/PVA/CS/AC.

Author Contributions: L.D., conceptualization, methodology, data analysis, and writing—review and editing; T.M.D.N., methodology, data collection, data analysis, and writing manuscript; T.M.L., data collection; K.G.H. data analysis and writing—review; T.P.T.Q. data analysis and writing—review and editing. All authors have read and agreed to the published version of the manuscript.

Funding: This research received no external funding.

Institutional Review Board Statement: Not applicable.

Informed Consent Statement: Not applicable.

Data Availability Statement: All data that support the findings of this study are included within the article.

Conflicts of Interest: The authors declare no conflict of interest.

Abbreviations

m	Mass of the Nanoparticles (g)
V	sample volume (mL)
C_0	initial concentration (mg/mL)
C_t	concentration at time t (mg/mL)
C_e	equilibrium aqueous-phase concentration adsorbate (mg/L)
Q_0	theoretical adsorption capacity (mg/g)
Q_e	amount of MB absorbed per unit mass of nanoparticle at the equilibrium (mg/g)
Q_t	amount of MB absorbed per unit mass of nanoparticle at time t (mg/g)
Q_m	quantity of adsorbate adsorbed in a single monolayer (mg/g)
α	Theoretical initial adsorption rate
β	Theoretical desorption rate
M_t	Released mass fraction at a time (t)
M_∞	The Amount of MB at Equilibrium State
θ	fractional surface coverage
X_2	Chi-square value
n_{KP}	Korsmeyer-Peppas release exponent factor
k_{KP}	Korsmeyer-Peppas release rate constant
k_H	Higuchi release rate constant
K_L	constant related to the free adsorption energy and the reciprocal of the concentration at which half saturation of the adsorbent is reached
k_0	Constant mass fraction at a time (t) release
k_1	Pseudo-first-order rate constant (s^{-1})
k_2	Pseudo-second-order rate constant (s^{-1})

k_a	Respective rate constant for adsorption
k_d	Respective rate constant for desorption

References

- Altohamy, R.; Ali, S.; Li, F.; Okasha, K.; Mahmoud, Y.; Elsamahy, T.; Jiao, H.; Fu, Y.; Sun, J. A Critical Review on the Treatment of Dye-Containing Wastewater: Ecotoxicological and Health Concerns of Textile Dyes and Possible Remediation Approaches for Environmental Safety. *Ecotoxicol. Environ. Saf.* **2022**, *231*, 113160. [\[CrossRef\]](#)
- Patel, H. Charcoal as an Adsorbent for Textile Wastewater Treatment. *Sep. Sci. Technol.* **2018**, *53*, 2797–2812. [\[CrossRef\]](#)
- Ali, H. Biodegradation of Synthetic Dyes—A Review. *Water. Air. Soil Pollut.* **2010**, *213*, 251–273. [\[CrossRef\]](#)
- Lellis, B.; Fávaro-Polonio, C.Z.; Pamphile, J.A.; Polonio, J.C. Effects of Textile Dyes on Health and the Environment and Bioremediation Potential of Living Organisms. *Biotechnol. Res. Innov.* **2019**, *3*, 275–290. [\[CrossRef\]](#)
- Laing, I.G. The Impact of Effluent Regulations on the Dyeing Industry. *Rev. Prog. Color. Relat. Top.* **1991**, *21*, 56–71. [\[CrossRef\]](#)
- Quach, T.P.T.; Doan, L. Surface Modifications of Superparamagnetic Iron Oxide Nanoparticles with Polyvinyl Alcohol, Chitosan, and Graphene Oxide as Methylene Blue Adsorbents. *Coatings* **2023**, *13*, 1333. [\[CrossRef\]](#)
- Damasceno, B.S.; da Silva, A.F.V.; de Araújo, A.C.V. Dye Adsorption onto Magnetic and Superparamagnetic Fe₃O₄ Nanoparticles: A Detailed Comparative Study. *J. Environ. Chem. Eng.* **2020**, *8*, 103994. [\[CrossRef\]](#)
- Atkins, P.; de Paula, J.; Friedman, R. *Physical Chemistry: Quanta, Matter, and Change*; OUP Oxford: Oxford, UK, 2014; ISBN 978-0-19-960981-9.
- Kumar, K.V.; Subanandam, K.; Bhagavanulu, D. Making GAC Sorption Economic. *Pollut. Res.* **2004**, *23*, 439–444.
- Bai, L.; Li, Z.; Zhang, Y.; Wang, T.; Lu, R.; Zhou, W.; Gao, H.; Zhang, S. Synthesis of Water-Dispersible Graphene-Modified Magnetic Polypyrrole Nanocomposite and Its Ability to Efficiently Adsorb Methylene Blue from Aqueous Solution. *Chem. Eng. J.* **2015**, *279*, 757–766. [\[CrossRef\]](#)
- Enriquez-Navas, P.M.; Garcia-Martin, M.L. Application of Inorganic Nanoparticles for Diagnosis Based on MRI. In *Frontiers of Nanoscience*; Elsevier: Amsterdam, The Netherlands, 2012; Volume 4, pp. 233–245, ISBN 978-0-12-415769-9.
- Chee, C.; Leo, B.F.; Lai, C.W. *Superparamagnetic Iron Oxide Nanoparticles for Drug Delivery*; Woodhead Publishing: Cambridge, UK, 2018; pp. 861–903, ISBN 978-0-12-813741-3.
- Mahmoudi, M.; Sant, S.; Wang, B.; Laurent, S.; Sen, T. Superparamagnetic Iron Oxide Nanoparticles (SPIONs): Development, Surface Modification and Applications in Chemotherapy. *Adv. Drug Deliv. Rev.* **2011**, *63*, 24–46. [\[CrossRef\]](#)
- Seabra, A.; Pelegrino, M.; Haddad, P. Antimicrobial Applications of Superparamagnetic Iron Oxide Nanoparticles. In *Nanostructures for Antimicrobial Therapy: Nanostructures in Therapeutic Medicine Series*; Elsevier: Amsterdam, The Netherlands, 2017; pp. 531–550, ISBN 978-0-323-46152-8.
- Liu, M.; Ye, Y.; Ye, J.; Gao, T.; Wang, D.; Chen, G.; Song, Z. Recent Advances of Magnetite (Fe₃O₄)-Based Magnetic Materials in Catalytic Applications. *Magnetochemistry* **2023**, *9*, 110. [\[CrossRef\]](#)
- Laurent, S.; Forge, D.; Port, M.; Roch, A.; Robic, C.; Vander Elst, L.; Muller, R.N. Magnetic Iron Oxide Nanoparticles: Synthesis, Stabilization, Vectorization, Physicochemical Characterizations, and Biological Applications. *Chem. Rev.* **2010**, *110*, 2574. [\[CrossRef\]](#)
- Doan, L. Surface Modifications of Superparamagnetic Iron Oxide Nanoparticles with Polyvinyl Alcohol and Activated Charcoal as Methylene Blue Adsorbents. *Magnetochemistry* **2023**, *9*, 211. [\[CrossRef\]](#)
- Llenas, M.; Sandoval, S.; Costa, P.M.; Oró-Solé, J.; Lope-Piedrafita, S.; Ballesteros, B.; Al-Jamal, K.T.; Tobias, G. Microwave-Assisted Synthesis of SPION-Reduced Graphene Oxide Hybrids for Magnetic Resonance Imaging (MRI). *Nanomaterials* **2019**, *9*, 1364. [\[CrossRef\]](#)
- Bertran, A.; Sandoval, S.; Oró-Solé, J.; Sánchez, À.; Tobias, G. Particle Size Determination from Magnetization Curves in Reduced Graphene Oxide Decorated with Monodispersed Superparamagnetic Iron Oxide Nanoparticles. *J. Colloid Interface Sci.* **2020**, *566*, 107–119. [\[CrossRef\]](#)
- Li, Z.; Sun, Y.; Xing, J.; Meng, A. Fast Removal of Methylene Blue by Fe₃O₄ Magnetic Nanoparticles and Their Cycling Property. *J. Nanosci. Nanotechnol.* **2019**, *19*, 2116–2123. [\[CrossRef\]](#)
- Habila, M.A.; Moshab, M.S.; El-Toni, A.M.; AlOthman, Z.A.; Badjah Hadj Ahmed, A.Y. Thermal Fabrication of Magnetic Fe₃O₄ (Nanoparticle)@Carbon Sheets from Waste Resources for the Adsorption of Dyes: Kinetic, Equilibrium, and UV-Visible Spectroscopy Investigations. *Nanomaterials* **2023**, *13*, 1266. [\[CrossRef\]](#)
- Yao, Y.; Miao, S.; Liu, S.; Ma, L.P.; Sun, H.; Wang, S. Synthesis, Characterization, and Adsorption Properties of Magnetic Fe₃O₄@graphene Nanocomposite. *Chem. Eng. J.* **2012**, *184*, 326–332. [\[CrossRef\]](#)
- Ahamad, T.; Naushad, M.; Eldesoky, G.E.; Al-Saeedi, S.I.; Nafady, A.; Al-Kadhi, N.S.; Al-Muhtaseb, A.H.; Khan, A.A.; Khan, A. Effective and Fast Adsorptive Removal of Toxic Cationic Dye (MB) from Aqueous Medium Using Amino-Functionalized Magnetic Multiwall Carbon Nanotubes. *J. Mol. Liq.* **2019**, *282*, 154–161. [\[CrossRef\]](#)
- Wu, K.-H.; Huang, W.-C.; Hung, W.-C.; Tsai, C.-W. Modified Expanded Graphite/Fe₃O₄ Composite as an Adsorbent of Methylene Blue: Adsorption Kinetics and Isotherms. *Mater. Sci. Eng. B* **2021**, *266*, 115068. [\[CrossRef\]](#)
- Tishbi, P.; Mosayebi, M.; Salehi, Z.; Fatemi, S.; Faegh, E. Synthesizing Magnetic Graphene Oxide Nanomaterial (GO-Fe₃O₄) and Kinetic Modelling of Methylene Blue Adsorption from Water. *Can. J. Chem. Eng.* **2022**, *100*, 3321–3334. [\[CrossRef\]](#)

26. Hingrajiya, R.D.; Patel, M.P. Fe₃O₄ Modified Chitosan Based Co-Polymeric Magnetic Composite Hydrogel: Synthesis, Characterization and Evaluation for the Removal of Methylene Blue from Aqueous Solutions. *Int. J. Biol. Macromol.* **2023**, *244*, 125251. [[CrossRef](#)] [[PubMed](#)]
27. Graphene Oxide/Fe₃O₄/Chitosan Nanocomposite: A Recoverable and Recyclable Adsorbent for Organic Dyes Removal. Application to Methylene Blue-IOPscience. Available online: <https://iopscience.iop.org/article/10.1088/2053-1591/aa6096/meta> (accessed on 13 September 2023).
28. Subhan, F.; Aslam, S.; Yan, Z.; Khan, M.; Etim, U.J.; Naeem, M. Effective Adsorptive Performance of Fe₃O₄@SiO₂ Core Shell Spheres for Methylene Blue: Kinetics, Isotherm and Mechanism. *J. Porous Mater.* **2019**, *26*, 1465–1474. [[CrossRef](#)]
29. Zhang, C.; Dai, Y.; Wu, Y.; Lu, G.; Cao, Z.; Cheng, J.; Wang, K.; Yang, H.; Xia, Y.; Wen, X.; et al. Facile Preparation of Polyacrylamide/Chitosan/Fe₃O₄ Composite Hydrogels for Effective Removal of Methylene Blue from Aqueous Solution. *Carbohydr. Polym.* **2020**, *234*, 115882. [[CrossRef](#)] [[PubMed](#)]
30. Ai, L.; Zhang, C.; Liao, F.; Wang, Y.; Li, M.; Meng, L.; Jiang, J. Removal of Methylene Blue from Aqueous Solution with Magnetite Loaded Multi-Wall Carbon Nanotube: Kinetic, Isotherm and Mechanism Analysis. *J. Hazard. Mater.* **2011**, *198*, 282–290. [[CrossRef](#)] [[PubMed](#)]
31. Doan, L. Surface Modifications of Superparamagnetic Iron Oxide Nanoparticles with Polyvinyl Alcohol and Graphite as Methylene Blue Adsorbents. *Coatings* **2023**, *13*, 1558. [[CrossRef](#)]
32. Zhang, W.; Zhang, L.; Zhao, X.; Zhou, Z. Citrus Pectin Derived Ultrasmall Fe₃O₄@C Nanoparticles as a High-Performance Adsorbent toward Removal of Methylene Blue. *J. Mol. Liq.* **2016**, *222*, 995–1002. [[CrossRef](#)]
33. Hameed, B.H.; Ahmad, A.L.; Latiff, K.N.A. Adsorption of Basic Dye (Methylene Blue) onto Activated Carbon Prepared from Rattan Sawdust. *Dye. Pigment.* **2007**, *75*, 143–149. [[CrossRef](#)]
34. Xue, H.; Wang, X.; Xu, Q.; Dhaouadi, F.; Sellaoui, L.; Seliem, M.K.; Ben Lamine, A.; Belmabrouk, H.; Bajahzar, A.; Bonilla-Petriciolet, A.; et al. Adsorption of Methylene Blue from Aqueous Solution on Activated Carbons and Composite Prepared from an Agricultural Waste Biomass: A Comparative Study by Experimental and Advanced Modeling Analysis. *Chem. Eng. J.* **2022**, *430*, 132801. [[CrossRef](#)]
35. Avom, J.; Mbadcam, J.K.; Noubactep, C.; Germain, P. Adsorption of Methylene Blue from an Aqueous Solution on to Activated Carbons from Palm-Tree Cobs. *Carbon* **1997**, *35*, 365–369. [[CrossRef](#)]
36. Thang, N.H.; Khang, D.S.; Hai, T.D.; Nga, D.T.; Tuan, P.D. Methylene Blue Adsorption Mechanism of Activated Carbon Synthesised from Cashew Nut Shells. *RSC Adv.* **2021**, *11*, 26563–26570. [[CrossRef](#)]
37. Kim, T.; Jung, G.; Yoo, S.; Suh, K.S.; Ruoff, R.S. Activated Graphene-Based Carbons as Supercapacitor Electrodes with Macro- and Mesopores. *ACS Nano* **2013**, *7*, 6899–6905. [[CrossRef](#)] [[PubMed](#)]
38. Nguyen, T.-T.-N.; He, J.-L. Preparation of Titanium Monoxide Nanopowder by Low-Energy Wet Ball-Milling. *Adv. Powder Technol.* **2016**, *27*, 1868–1873. [[CrossRef](#)]
39. Tran, D.N.H.; Kabiri, S.; Wang, L.; Losic, D. Engineered Graphene–Nanoparticle Aerogel Composites for Efficient Removal of Phosphate from Water. *J. Mater. Chem. A* **2015**, *3*, 6844–6852. [[CrossRef](#)]
40. Moo, J.G.S.; Khezri, B.; Webster, R.D.; Pumera, M. Graphene Oxides Prepared by Hummers’, Hofmann’s, and Staudenmaier’s Methods: Dramatic Influences on Heavy-Metal-Ion Adsorption. *ChemPhysChem* **2014**, *15*, 2922–2929. [[CrossRef](#)]
41. Li, Y.; Van Zijll, M.; Chiang, S.; Pan, N. KOH Modified Graphene Nanosheets for Supercapacitor Electrodes. *J. Power Sources* **2011**, *196*, 6003–6006. [[CrossRef](#)]
42. Chung, D.D.L. Review Graphite. *J. Mater. Sci.* **2002**, *37*, 1475–1489. [[CrossRef](#)]
43. Zhao, M.; Liu, P. Adsorption of Methylene Blue from Aqueous Solutions by Modified Expanded Graphite Powder. *Desalination* **2009**, *249*, 331–336. [[CrossRef](#)]
44. Senthilkumaar, S.; Varadarajan, P.R.; Porkodi, K.; Subbhuraam, C.V. Adsorption of Methylene Blue onto Jute Fiber Carbon: Kinetics and Equilibrium Studies. *J. Colloid Interface Sci.* **2005**, *284*, 78–82. [[CrossRef](#)]
45. Kumar, P.S.; Ramalingam, S.; Sathishkumar, K. Removal of Methylene Blue Dye from Aqueous Solution by Activated Carbon Prepared from Cashew Nut Shell as a New Low-Cost Adsorbent. *Korean J. Chem. Eng.* **2011**, *28*, 149–155. [[CrossRef](#)]
46. Altundag, H.; Bina, E.; Altintig, E. The Levels of Trace Elements in Honey and Molasses Samples That Were Determined by ICP-OES After Microwave Digestion Method. *Biol. Trace Elem. Res.* **2016**, *170*, 508–514. [[CrossRef](#)]
47. Le, T.D.; Tran, L.T.; Dang, H.T.M.; Tran, T.T.H.; Tran, H.V. Graphene Oxide/Polyvinyl Alcohol/Fe₃O₄ Nanocomposite: An Efficient Adsorbent for Co(II) Ion Removal. *J. Anal. Methods Chem.* **2021**, *2021*, e6670913. [[CrossRef](#)]
48. Doan, L.; Lu, Y.; Karatela, M.; Phan, V.; Jeffryes, C.; Benson, T.; Wujcik, E.K. Surface Modifications of Superparamagnetic Iron Oxide Nanoparticles with Polylactic Acid-Polyethylene Glycol Diblock Copolymer and Graphene Oxide for a Protein Delivery Vehicle. *Eng. Sci.* **2019**, *7*, 10–16. [[CrossRef](#)]
49. Pandey, N.; Surana, S.; Shukla, S.K.; Singh, N.B. Methylene Blue Removal on Nano-Fe₃O₄/Poly(Vinyl Alcohol)/Polyacrylamide Hydrogel. *Emerg. Mater. Res.* **2017**, *6*, 305–313. [[CrossRef](#)]
50. Adamczuk, A.; Kołodyńska, D. Equilibrium, Thermodynamic and Kinetic Studies on Removal of Chromium, Copper, Zinc and Arsenic from Aqueous Solutions onto Fly Ash Coated by Chitosan. *Chem. Eng. J.* **2015**, *274*, 200–212. [[CrossRef](#)]
51. Javanbakht, V.; Ghoreishi, S.M.; Habibi, N.; Javanbakht, M. A Novel Magnetic Chitosan/Clinoptilolite/Magnetite Nanocomposite for Highly Efficient Removal of Pb(II) Ions from Aqueous Solution. *Powder Technol.* **2016**, *302*, 372–383. [[CrossRef](#)]

52. Liu, N.; Chen, X.-G.; Park, H.-J.; Liu, C.-G.; Liu, C.-S.; Meng, X.-H.; Yu, L.-J. Effect of MW and Concentration of Chitosan on Antibacterial Activity of *Escherichia coli*. *Carbohydr. Polym.* **2006**, *64*, 60–65. [[CrossRef](#)]
53. Doan, L.; Tran, K. Relationship between the Polymer Blend Using Chitosan, Polyethylene Glycol, Polyvinyl Alcohol, Polyvinylpyrrolidone, and Antimicrobial Activities against *Staphylococcus aureus*. *Pharmaceutics* **2023**, *15*, 2453. [[CrossRef](#)]
54. Liu, Q.; Yang, B.; Zhang, L.; Huang, R. Adsorptive Removal of Cr(VI) from Aqueous Solutions by Cross-Linked Chitosan/Bentonite Composite. *Korean J. Chem. Eng.* **2015**, *32*, 1314–1322. [[CrossRef](#)]
55. Nechita, P. Applications of Chitosan in Wastewater Treatment. In *Biological Activities and Application of Marine Polysaccharides*; IntechOpen: Rijeka, Croatia, 2017; ISBN 978-953-51-2860-1.
56. Liu, H.; Du, Y.; Wang, X.; Sun, L. Chitosan Kills Bacteria through Cell Membrane Damage. *Int. J. Food Microbiol.* **2004**, *95*, 147–155. [[CrossRef](#)]
57. Lou, M.-M.; Zhu, B.; Muhammad, I.; Li, B.; Xie, G.-L.; Wang, Y.-L.; Li, H.-Y.; Sun, G.-C. Antibacterial Activity and Mechanism of Action of Chitosan Solutions against Apricot Fruit Rot Pathogen *Burkholderia Seminalis*. *Carbohydr. Res.* **2011**, *346*, 1294–1301. [[CrossRef](#)] [[PubMed](#)]
58. Ma, Z.; Kim, D.; Adesogan, A.T.; Ko, S.; Galvao, K.; Jeong, K.C. Chitosan Microparticles Exert Broad-Spectrum Antimicrobial Activity against Antibiotic-Resistant Micro-Organisms without Increasing Resistance. *ACS Appl. Mater. Interfaces* **2016**, *8*, 10700–10709. [[CrossRef](#)]
59. Kamjumphol, W.; Chareonsudjai, P.; Chareonsudjai, S. Antibacterial Activity of Chitosan against *Burkholderia pseudomallei*. *MicrobiologyOpen* **2018**, *7*, e00534. [[CrossRef](#)] [[PubMed](#)]
60. Doble, M.; Kumar, A. Degradation of Polymers. In *Biotreatment of Industrial Effluents*; Elsevier: Amsterdam, The Netherlands, 2005; pp. 101–110, ISBN 978-0-7506-7838-4.
61. Jia, Z.; Li, Z.; Li, S.; Li, Y.; Zhu, R. Adsorption Performance and Mechanism of Methylene Blue on Chemically Activated Carbon Spheres Derived from Hydrothermally-Prepared Poly(Vinyl Alcohol) Microspheres. *J. Mol. Liq.* **2016**, *220*, 56–62. [[CrossRef](#)]
62. Kim, J.O.; Park, J.K.; Kim, J.H.; Jin, S.G.; Yong, C.S.; Li, D.X.; Choi, J.Y.; Woo, J.S.; Yoo, B.K.; Lyoo, W.S.; et al. Development of Polyvinyl Alcohol–Sodium Alginate Gel-Matrix-Based Wound Dressing System Containing Nitrofurazone. *Int. J. Pharm.* **2008**, *359*, 79–86. [[CrossRef](#)] [[PubMed](#)]
63. Jin, J.; Song, M.; Hourston, D.J. Novel Chitosan-Based Films Cross-Linked by Genipin with Improved Physical Properties. *Biomacromolecules* **2004**, *5*, 162–168. [[CrossRef](#)]
64. Millon, L.E.; Wan, W.K. The Polyvinyl Alcohol–Bacterial Cellulose System as a New Nanocomposite for Biomedical Applications. *J. Biomed. Mater. Res. B Appl. Biomater.* **2006**, *79B*, 245–253. [[CrossRef](#)]
65. Schmedlen, R.H.; Masters, K.S.; West, J.L. Photocrosslinkable Polyvinyl Alcohol Hydrogels That Can Be Modified with Cell Adhesion Peptides for Use in Tissue Engineering. *Biomaterials* **2002**, *23*, 4325–4332. [[CrossRef](#)]
66. Jain, N.; Singh, V.K.; Chauhan, S. A Review on Mechanical and Water Absorption Properties of Polyvinyl Alcohol Based Composites/Films. *J. Mech. Behav. Mater.* **2017**, *26*, 213–222. [[CrossRef](#)]
67. Venkataprasanna, K.S.; Prakash, J.; Vignesh, S.; Bharath, G.; Venkatesan, M.; Banat, F.; Sahabudeen, S.; Ramachandran, S.; Devanand Venkatasubbu, G. Fabrication of Chitosan/PVA/GO/CuO Patch for Potential Wound Healing Application. *Int. J. Biol. Macromol.* **2020**, *143*, 744–762. [[CrossRef](#)]
68. El-Hefian, E.A.; Nasef, M.M.; Yahaya, A.H. The Preparation and Characterization of Chitosan/Poly (Vinyl Alcohol) Blended Films. *E-J. Chem.* **2010**, *7*, 1212–1219. [[CrossRef](#)]
69. Liu, Y.; Wang, S.; Lan, W. Fabrication of Antibacterial Chitosan-PVA Blended Film Using Electrospray Technique for Food Packaging Applications. *Int. J. Biol. Macromol.* **2018**, *107*, 848–854. [[CrossRef](#)]
70. Saragi, T.; Depi, B.L.; Butarbutar, S.; Permana, B.; Risdiana. The Impact of Synthesis Temperature on Magnetite Nanoparticles Size Synthesized by Co-Precipitation Method. *J. Phys. Conf. Ser.* **2018**, *1013*, 012190. [[CrossRef](#)]
71. Zhao, Y.; Qiu, Z.; Huang, J. Preparation and Analysis of Fe₃O₄ Magnetic Nanoparticles Used as Targeted-Drug Carriers. *Chin. J. Chem. Eng.* **2008**, *16*, 451–455. [[CrossRef](#)]
72. Doan, L. Modifying Superparamagnetic Iron Oxide Nanoparticles as Methylene Blue Adsorbents: A Review. *ChemEngineering* **2023**, *7*, 77. [[CrossRef](#)]
73. Jalilian, A.R.; Panahifar, A.; Mahmoudi, M.; Akhlaghi, M.; Simchi, A. Preparation and Biological Evaluation of [67Ga]-Labeled-Superparamagnetic Nanoparticles in Normal Rats. *Radiochim. Acta* **2009**, *97*, 51–56. [[CrossRef](#)]
74. Wahajuddin, N.; Arora, S. Arora Superparamagnetic Iron Oxide Nanoparticles: Magnetic Nanoplatfoms as Drug Carriers. *Int. J. Nanomed.* **2012**, *7*, 3445–3471. [[CrossRef](#)]
75. Mohapatra, S.; Mallick, S.K.; Maiti, T.K.; Ghosh, S.K.; Pramanik, P. Synthesis of Highly Stable Folic Acid Conjugated Magnetite Nanoparticles for Targeting Cancer Cells. *Nanotechnology* **2007**, *18*, 385102. [[CrossRef](#)]
76. Bellamy, L.J. *The Infrared Spectra of Complex Molecules*; Springer: Dordrecht, The Netherlands, 1980; ISBN 978-94-011-6522-8.
77. Franca, T.; Goncalves, D.; Cena, C. ATR-FTIR Spectroscopy Combined with Machine Learning for Classification of PVA/PVP Blends in Low Concentration. *Vib. Spectrosc.* **2022**, *120*, 103378. [[CrossRef](#)]
78. Abureesh, M.A.; Oladipo, A.A.; Gazi, M. Facile Synthesis of Glucose-Sensitive Chitosan–Poly(Vinyl Alcohol) Hydrogel: Drug Release Optimization and Swelling Properties. *Int. J. Biol. Macromol.* **2016**, *90*, 75–80. [[CrossRef](#)]

79. Mansur, H.S.; Sadahira, C.M.; Souza, A.N.; Mansur, A.A.P. FTIR Spectroscopy Characterization of Poly (Vinyl Alcohol) Hydrogel with Different Hydrolysis Degree and Chemically Crosslinked with Glutaraldehyde. *Mater. Sci. Eng. C* **2008**, *28*, 539–548. [[CrossRef](#)]
80. Jipa, I.; Stoica, A.; Stroescu, M.; Dobre, L.-M.; Dobre, T.; Jinga, S.; Tardei, C. Potassium Sorbate Release from Poly(Vinyl Alcohol)-Bacterial Cellulose Films. *Chem. Pap.* **2012**, *66*, 138–143. [[CrossRef](#)]
81. Reis, E.F.D.; Campos, F.S.; Lage, A.P.; Leite, R.C.; Heneine, L.G.; Vasconcelos, W.L.; Lobato, Z.I.P.; Mansur, H.S. Synthesis and Characterization of Poly (Vinyl Alcohol) Hydrogels and Hybrids for rMPB70 Protein Adsorption. *Mater. Res.* **2006**, *9*, 185–191. [[CrossRef](#)]
82. Kharazmi, A.; Faraji, N.; Mat Hussin, R.; Saion, E.; Yunus, W.M.M.; Behzad, K. Structural, Optical, Opto-Thermal and Thermal Properties of ZnS–PVA Nanofluids Synthesized through a Radiolytic Approach. *Beilstein J. Nanotechnol.* **2015**, *6*, 529–536. [[CrossRef](#)] [[PubMed](#)]
83. Jabbar, W.A.; Habubi, N.F.; Chiad, S.S. Optical Characterization of Silver Doped Poly (Vinyl Alcohol) Films. *J. Ark. Acad. Sci.* **2010**, *64*, 21.
84. Dibbern-Brunelli, D.; Atvars, T.D.Z.; Joekes, I.; Barbosa, V.C. Mapping Phases of Poly(Vinyl Alcohol) and Poly(Vinyl Acetate) Blends by FTIR Microspectroscopy and Optical Fluorescence Microscopy. *J. Appl. Polym. Sci.* **1998**, *69*, 645–655. [[CrossRef](#)]
85. Tretinnikov, O.N.; Zagorskaya, S.A. Determination of the Degree of Crystallinity of Poly(Vinyl Alcohol) by FTIR Spectroscopy. *J. Appl. Spectrosc.* **2012**, *79*, 521–526. [[CrossRef](#)]
86. Fernandes Queiroz, M.; Melo, K.; Sabry, D.; Sassaki, G.; Rocha, H. Does the Use of Chitosan Contribute to Oxalate Kidney Stone Formation? *Mar. Drugs* **2014**, *13*, 141–158. [[CrossRef](#)]
87. Varma, R.; Vasudevan, S. Extraction, Characterization, and Antimicrobial Activity of Chitosan from Horse Mussel *Modiolus Modiolus*. *ACS Omega* **2020**, *5*, 20224–20230. [[CrossRef](#)]
88. Yasmeen, S.; Kabiraz, M.; Saha, B.; Qadir, M.; Gafur, M.; Masum, S. Chromium (VI) Ions Removal from Tannery Effluent Using Chitosan-Microcrystalline Cellulose Composite as Adsorbent. *Int. Res. J. Pure Appl. Chem.* **2016**, *10*, 1–14. [[CrossRef](#)]
89. Dhumale, V.A.; Gangwar, R.K.; Datar, S.S.; Sharma, R.B. Reversible Aggregation Control of Polyvinylpyrrolidone Capped Gold Nanoparticles as a Function of pH. *Mater. Express* **2012**, *2*, 311–318. [[CrossRef](#)]
90. Hashim, N.; Adnan, N.; Hassan, L.; Abdullah, S.; Aniyah, N.; Sobri, M. Extraction of Degradable Biopolymer Material from Shrimp Shell. *IOP Conf. Ser. Mater. Sci. Eng.* **2022**, *3*, 58–64.
91. Stoica, A.; Dobre, L.; Stroescu, M.; Deleanu, I. Fourier Transform Infrared (FTIR) Spectroscopy for Characterization of Antimicrobial Films Containing Chitosan. *Ann. Univ. Oradea Fasc.* **2010**, *2010*, 1234–1240.
92. Wang, M.; Zhang, J.; Zhao, H.; Deng, W.; Lu, J.; Ye, Q. Enhancement of Oxidation Capacity of ZVI/Cu²⁺/PMS Systems by Weak Magnetic Fields. *Desalination Water Treat.* **2019**, *161*, 260–268. [[CrossRef](#)]
93. Tang, C.; Shu, Y.; Zhang, R.; Li, X.; Song, J.; Li, B.; Zhang, Y.; Ou, D. Comparison of the Removal and Adsorption Mechanisms of Cadmium and Lead from Aqueous Solution by Activated Carbons Prepared from Typha Angustifolia and Salix Matsudana. *RSC Adv.* **2017**, *7*, 16092–16103. [[CrossRef](#)]
94. Maulina, S.; Mentari, V.A. Comparison of Functional Group and Morphological Surface of Activated Carbon from Oil Palm Fronds Using Phosphoric Acid (H₃PO₄) and Nitric Acid (HNO₃) as an Activator. *IOP Conf. Ser. Mater. Sci. Eng.* **2019**, *505*, 012023. [[CrossRef](#)]
95. Allwar, A. Preparation and Characteristics of Activated Carbon from Oil Palm Shell for Removal of Iron and Copper from Patchouli Oil. *Int. J. Appl. Chem.* **2016**, *12*, 183–192.
96. Bera, M.; Chandravati; Gupta, P.; Maji, P.K. Facile One-Pot Synthesis of Graphene Oxide by Sonication Assisted Mechanochemical Approach and Its Surface Chemistry. *J. Nanosci. Nanotechnol.* **2018**, *18*, 902–912. [[CrossRef](#)]
97. Kartick, B.; Srivastava, S.K.; Srivastava, A.I. Green Synthesis of Graphene. *J. Nanosci. Nanotechnol.* **2013**, *13*, 4320–4324. [[CrossRef](#)] [[PubMed](#)]
98. Rochman, R.A.; Wahyuningsih, S.; Ramelan, A.H.; Hanif, Q.A. Preparation of Nitrogen and Sulphur Co-Doped Reduced Graphene Oxide (rGO-NS) Using N and S Heteroatom of Thiourea. *IOP Conf. Ser. Mater. Sci. Eng.* **2019**, *509*, 012119. [[CrossRef](#)]
99. Visca, R.; Dewi, M.N.; Liviani, A.; Satriawan, B.D. Characterization of FTIR in Graphite from Palm Oil Waste with Ferric Chloride Catalyst. *Interdiscip. Soc. Stud.* **2022**, *1*, 11. [[CrossRef](#)]
100. Shalaby, T.I.; Fikrt, N.M.; Mohamed, M.M.; El Kady, M.F. Preparation and Characterization of Iron Oxide Nanoparticles Coated with Chitosan for Removal of Cd(II) and Cr(VI) from Aqueous Solution. *Water Sci. Technol.* **2014**, *70*, 1004–1010. [[CrossRef](#)]
101. Zhao, D.-L.; Teng, P.; Xu, Y.; Xia, Q.-S.; Tang, J.-T. Magnetic and Inductive Heating Properties of Fe₃O₄/Polyethylene Glycol Composite Nanoparticles with Core–Shell Structure. *J. Alloys Compd.* **2010**, *502*, 392–395. [[CrossRef](#)]
102. Sayahi, M.H.; Sepahdar, A.; Bazrafkan, F.; Dehghani, F.; Mahdavi, M.; Bahadorikhalili, S. Ionic Liquid Modified SPION@Chitosan as a Novel and Reusable Superparamagnetic Catalyst for Green One-Pot Synthesis of Pyrido[2,3-*d*]pyrimidine-dione Derivatives in Water. *Catalysts* **2023**, *13*, 290. [[CrossRef](#)]
103. Maldonado-Camargo, L.; Unni, M.; Rinaldi, C. Magnetic Characterization of Iron Oxide Nanoparticles for Biomedical Applications. In *Biomedical Nanotechnology*; Petrosko, S.H., Day, E.S., Eds.; Methods in Molecular Biology; Springer New York: New York, NY, USA, 2017; Volume 1570, pp. 47–71, ISBN 978-1-4939-6838-1.

104. Yurdakal, S.; Garlisi, C.; Özcan, L.; Bellardita, M.; Palmisano, G. Chapter 4-(Photo)Catalyst Characterization Techniques: Adsorption Isotherms and BET, SEM, FTIR, UV-Vis, Photoluminescence, and Electrochemical Characterizations. In *Heterogeneous Photocatalysis*; Marci, G., Palmisano, L., Eds.; Elsevier: Amsterdam, The Netherlands, 2019; pp. 87–152, ISBN 978-0-444-64015-4.
105. Characterization of the Adsorption Site Energies and Heterogeneous Surfaces of Porous Materials—Journal of Materials Chemistry A (RSC Publishing). Available online: <https://pubs.rsc.org/en/content/articlelanding/2019/TA/C9TA00287A> (accessed on 18 September 2023).
106. Dai, H.; Huang, Y.; Huang, H. Eco-Friendly Polyvinyl Alcohol/Carboxymethyl Cellulose Hydrogels Reinforced with Graphene Oxide and Bentonite for Enhanced Adsorption of Methylene Blue. *Carbohydr. Polym.* **2018**, *185*, 1–11. [[CrossRef](#)]
107. Sharma, G.; Kumar, A.; Devi, K.; Sharma, S.; Naushad, M.; Ghfar, A.A.; Ahamad, T.; Stadler, F.J. Guar Gum-Crosslinked-Soya Lecithin Nanohydrogel Sheets as Effective Adsorbent for the Removal of Thiophanate Methyl Fungicide. *Int. J. Biol. Macromol.* **2018**, *114*, 295–305. [[CrossRef](#)] [[PubMed](#)]
108. Sharma, G.; Kumar, A.; Naushad, M.; García-Peñas, A.; Al-Muhtaseb, A.H.; Ghfar, A.A.; Sharma, V.; Ahamad, T.; Stadler, F.J. Fabrication and Characterization of Gum Arabic-Cl-Poly(Acrylamide) Nanohydrogel for Effective Adsorption of Crystal Violet Dye. *Carbohydr. Polym.* **2018**, *202*, 444–453. [[CrossRef](#)] [[PubMed](#)]
109. Kannan, N.; Sundaram, M.M. Kinetics and Mechanism of Removal of Methylene Blue by Adsorption on Various Carbons—A Comparative Study. *Dye. Pigment.* **2001**, *51*, 25–40. [[CrossRef](#)]
110. Jawad, A.H.; Mohd Firdaus Hum, N.N.; Abdulhameed, A.S.; Mohd Ishak, M.A. Mesoporous Activated Carbon from Grass Waste via H₃PO₄-Activation for Methylene Blue Dye Removal: Modelling, Optimisation, and Mechanism Study. *Int. J. Environ. Anal. Chem.* **2022**, *102*, 6061–6077. [[CrossRef](#)]
111. Shikuku, V.O.; Zanella, R.; Kowenje, C.O.; Donato, F.F.; Bandeira, N.M.G.; Prestes, O.D. Single and Binary Adsorption of Sulfonamide Antibiotics onto Iron-Modified Clay: Linear and Nonlinear Isotherms, Kinetics, Thermodynamics, and Mechanistic Studies. *Appl. Water Sci.* **2018**, *8*, 175. [[CrossRef](#)]
112. Liu, L.; Luo, X.-B.; Ding, L.; Luo, S.-L. 4-Application of Nanotechnology in the Removal of Heavy Metal From Water. In *Nanomaterials for the Removal of Pollutants and Resource Reutilization*; Luo, X., Deng, F., Eds.; Micro and Nano Technologies; Elsevier: Amsterdam, The Netherlands, 2019; pp. 83–147, ISBN 978-0-12-814837-2.
113. Reed, B.E.; Matsumoto, M.R. Modeling Cadmium Adsorption by Activated Carbon Using the Langmuir and Freundlich Isotherm Expressions. *Sep. Sci. Technol.* **1993**, *28*, 2179–2195. [[CrossRef](#)]
114. Yao, Y.; Xu, F.; Chen, M.; Xu, Z.; Zhu, Z. Adsorption Behavior of Methylene Blue on Carbon Nanotubes. *Bioresour. Technol.* **2010**, *101*, 3040–3046. [[CrossRef](#)] [[PubMed](#)]

Disclaimer/Publisher’s Note: The statements, opinions and data contained in all publications are solely those of the individual author(s) and contributor(s) and not of MDPI and/or the editor(s). MDPI and/or the editor(s) disclaim responsibility for any injury to people or property resulting from any ideas, methods, instructions or products referred to in the content.